Norwegian University
of Life Sciences

Detection of root and butt rot in Norway Spruce (*Picea Abies*) using airborne hyperspectral images and laser scanning

Erik Armand Iversen

Forestry

I

Acknowledgments

Norwegian University of Life Sciences

Ås, 31.05.2020

Erik Armand Iversen

Abstract

The forest is an important renewable resource in a sustainable bioeconomy. Yearly, fungal decay causes economical losses that exceed 100 million NOK within the Norwegian forest sector. Root and butt rots are the main contributors and *Heterobasidion spp.* and *Armillaria spp.* are the most common fungi registered. Norway spruce (*Picea abies* (L.) Karst.) is Norway's most significant commercial tree species and is especially exposed to infections from pathogenic fungi. It is estimated that one out of four spruce trees is infected at final felling. Infected trees are difficult to map over large areas as they show few external symptoms, and only manual methods currently exist. With future climate change, the extent of the damage is expected to increase, and new methods need to be developed which can detect rot with high accuracy over large areas. The spectral signature of trees can reveal information about plant health and laser data can be used to segment individual trees. A combination of airborne hyperspectral images and laser scanning was used to develop logistic regression and random forest models capable of predicting rot in spruce. Laser data were used to create individual tree crowns (ITC) from which hyperspectral pixels were extracted. The visible, near-infrared (NIR) and infrared (IR) parts of the electromagnetic spectrum were analyzed (400-2500 nm) with data from a VNIR and SWIR sensor. There were partial significant differences between healthy and infected trees in the spectrum, but a defined rule to separate them was difficult to establish. Additionally, significant wavelengths are not easily comparable with similar studies, as many factors can affect the hyperspectral images. Significant wavelengths from all parts of the analyzed spectrum were incorporated into the models. Mean prediction accuracy was 63%, which is a modest improvement from previous research. The inclusion of laser data did improve the results, but the implementation needs to be further addressed. As continuous advances within hyperspectral sensors are made, the combination of airborne hyperspectral images and laser scanning to detect rot in spruce forests with high accuracy is promising.

Sammendrag

Skogen er en viktig fornybar ressurs i en bærekraftig bioøkonomi. Årlig forårsaker råteskader økonomiske tap som overstiger 100 millioner NOK innenfor den norske skogsektoren. Rotråte er den største bidragsyteren hvor *Heterobasidion spp.* og *Armillaria spp.* er de vanligste råtesoppene registrert. Gran (*Picea abies* (L.) Karst.) er Norges viktigste kommersielle treslag og er spesielt utsatt for angrep fra råtesopper. Det er estimert at en av fire grantrær er infisert ved slutthogst. Det er vanskelig å kartlegge infiserte trær ettersom de viser få eksterne symptomer, og det eksisterer kun manuelle metoder foreløpig. Med framtidige klimaendringer er det forventet at omfanget av skadene kommer til å øke, og det er behov for å utvikle nye metoder som kan detektere råte med høy nøyaktighet over større områder. Spektralsignaturen til et tre kan avsløre informasjon om plantehelse og laser data kan benyttes til å segmentere individuelle trær. En kombinasjon av flybåren hyperspektrale bilder og laserskanning ble benyttet til å utvikle logistisk regresjon og random forest modeller. Laser data ble brukt til å lage individuelle trekroner (ITC) som hyperspektral piksler ble ekstrahert fra. De synlige, nær infrarød (NIR) og infrarøde (IR) delene av det elektromagnetiske spekteret ble analysert (400-2500 nm) med data fra en VNIR og SWIR sensor. Delvis var det signifikante forskjeller mellom friske og infiserte trær i spekteret, men en definert regel for å skille mellom disse var vanskelig å etablere. Videre er signifikante bølgelengder lite sammenlignbare med lignende studier ettersom mange faktorer kan påvirke hyperspektrale bilder. Signifikante bølgelengder fra alle deler av det analyserte spekteret bli inkorporert i modellene. Gjennomsnittlig prediksjonsnøyaktighet var 63% som er en beskjeden forbedring fra tidligere forskning. Inkluderingen av laser data førte til en forbedring av resultatene, men implementering må adresseres ytterligere. Kontinuerlige fremskritt innen hyperspektrale sensorer gjør at kombinasjonen av flybåren hyperspektrale bilder og laserskanning til å detektere råte i granskog med høy nøyaktighet ser lovende ut.

Table of contents

Introduction

Background

The forest is a formidable renewable resource with vast potential for the future of a sustainable society. In a prospective world where its dependency on oil is gradually replaced by renewable resources, the importance of the forest will only increase. During the last decade, there has been a large focus on the "green shift" towards an eco-friendlier bioeconomy in Norway. The forest industry is a fundamental part of this new direction, which the Norwegian government recognizes. In the national strategy for the forest industry, it is stated that the forest industry will play a crucial part in a more sustainable economy, and the government wants to facilitate future development (Ministry of Agriculture and Food, 2015). With its increasing importance, the forest must be managed optimally, and its resources utilized accordingly.

The forest industry is already an essential part of Norway's economy in large parts of the country. It is important to settlement, employment and business development. The forest industry needs to be active, profitable and competitive to maintain its position of importance and to profit from the potential in its increased value creation (Ministry of Agriculture and Food, 2018). The forest area in Norway is 12 million ha, where 8.6 million ha is considered productive forest (Breidenbach et al., 2018). The growing stock has tripled from 1925 to 2014, and the last update from the Norwegian National Forest Inventory (NFI) estimated total growing stock of 9.7 billion m^3 in 2018 (Statistisk Sentralbyrå, 2018). Over the last decade, the commercial harvest of timber has seen a steady increase. Norway spruce (*Picea abies* (L.) Karst.) has been the most important commercial tree species during this period, and has accounted for roughly 2/3 of the total commercial harvest of timber (Norwegian Agriculture Agency, 2020). In 2019 forest owners sold 11 million m^3 roundwood to industry with an estimated value close to 5 billion NOK (Statistisk Sentralbyrå, 2020).

Buyers and sellers of roundwood designated for industry or export are obligated by Norwegian law to take measurements of the roundwood (Skogbrukslova, 2005). The measurement of roundwood is usually performed by Norsk Virkesmåling (2018), which acts as a neutral third-party between sellers and buyers of industrial roundwood, biofuel and chips in Norway. The value of industrial roundwood is based on their evaluation. By their regulations, industrial roundwood is either classified as a sawlog, or pulpwood, with subcategories based on different

parameters for quality and dimensions (Norsk Virkesmåling, 2015a; Norsk Virkesmåling, 2015b). Between the two, sawlogs are significantly more valuable. In 2019, the average price for sawlogs was 517 NOK/m^3 compared to 350 NOK/m^3 for pulpwood (Norwegian Agriculture Agency, 2020). If the roundwood doesn't meet the requirements for a sawlog, it is usually degraded to pulpwood. If the standards for neither category are met, the roundwood is rejected and considered a loss for the seller. The presence of rot is one of the quality parameters which roundwood is evaluated after that can lead to both degradation and rejection. In sawlogs, rot cannot be present, and it must be removed by shortening the length of the log. If the shortening exceeds 0.6 m, the entire log is rejected (Norsk Virkesmåling, 2015b). Rot is allowed in pulpwood but is limited to the overall prevalence at the ends of the log. In the lowest subcategory, the maximum prevalence is 70% of the diameter and 50% of the area (Norsk Virkesmåling, 2015a). The yearly economic loss from rot in Norway is estimated to exceed 100 million NOK, and the collective loss for Europe is estimated to be around 7.5 billion NOK (Dalen, 2018). There are considerable uncertainties related to these estimates though, considering shifts in the environment, market and political landscape (Thor, 2005)**.** In any case, there is no doubt that rot contributes to a significant economic loss on a yearly basis within the forest sector.

Prevalence of root and butt rot in spruce

Rot can be defined as the decomposition of organic material caused by fungal decay. The fungus produces enzymes that can decompose the organic material in wood. Depending on the fungus present, different organic materials are affected. Cellulose, hemicellulose and lignin are the main structural components in wood. The position of decay in the tree, and the affected wood components, is categorical for the rot. Root and butt rot is a common term for fungi that typically operate within this named group.

Growth and quality can be negatively affected by rot, and spruce is especially exposed to infections by pathogenic fungi (Solheim, 2010). Additionally, mortality increases. In prolonged infections, some fungi are capable of killing trees. Aside from trees dying directly from the infection itself, they are more exposed to windthrows as the wood structure is weakened. The proportion of decay in a forest impacts its stability, making trees vulnerable during storms (Hanssen et al., 2019). This reduces the total production of roundwood and is a considerable problem given its significance as a commercial tree species. NFI has carried out

multiple surveys that investigate the prevalence of rot in spruce forests. During the period 1964-1976, a survey found that 7.9% of the forests were infected by rot (Huse, 1983). A survey from the period 1982-1986 showed a larger degree of rot, with 9.3% of spruce forests being infected south of Saltfjellet (Solheim & Holen, 1990). Rot was identified from core samples taken at breast height in these surveys. The results can thus be misleading, as various studies show that core samples taken at breast height can underestimate the prevalence of rot in stumps by over 50% (Stenlid & Wästerlund, 1986; Thor, 2005). This is illustrated in Huse et al. (1994) where they studied the presence of root and butt rot in spruce stumps. The study was nationwide and included samples from 5000 different forest owners. The forest owners were given instructions to inspect and identify rot in stumps after clear-cutting. Of the examined stumps, 27% showed signs of visible rot, and it was most prevalent in the eastern parts of Norway. Multiple factors can contribute to the occurrence of rot in a forest. Thor et al. (2005) found that the frequency of rot increased with stand age, site index and altitudes above 100 m. Soil and bedrock properties have also shown to affect the occurrence of rot (Solheim, 2010).

Two main fungi cause root and butt rot in spruce in Norway; *Heterobasidion spp.* and *Armillaria spp.* (Næsvold, 1989; Solheim, 2010). *Heterobasidion spp.* is divided into two subspecies that differ concerning distribution and host tree. *H. parviporum* which mainly infects spruce and is common throughout the eastern parts of Norway, stretching from the south and up to Saltfjellet. *H. annosum* which has Scots pine (*Pinus sylvestris* L.) as its primary host, but can also infect spruce and broad-leaved trees, and is most common in the western parts of Norway (Fjærli, 2016; Solheim, 2010). *Armillaria spp.* can infect all wooden species, including coniferous and broad-leaved trees. Four types are known to occur in Norway, but only two are prevalent. These are *A. borealis* and *A. cepistipes* and they share a similar appearance. Both can be found all over Norway but the former is more common (Solheim, 2010). In a nationwide study by Huse et al. (1994), the most common fungi were *H. parviporum* 71% and *Armillaria spp.* 28%. Both appearing either alone or in combination with other fungi. There was a higher tendency for rot within older forests, but no correlation with altitude was found. This coincides with a probability model for rot in spruce forests developed by Granhus and Hylen (2016). The model predicts a higher probability of rot with increasing age and diameter. The results also substantiate *H. parviporum* as the dominant and most important fungus to cause rot in spruce (Solheim et al., 2012). Solheim (2010) estimates that on average, every fourth tree is infected by rot at final felling and *Heterobasidion spp.* is behind 80% of the cases. In a report from the Norwegian Institute of Bioeconomy Research (NIBIO) (Hanssen et al., 2019), it is expected

that the extent of the damage from *Heterobasidion spp.* and *Armillaria spp.* will increase with future climate change.

Bjørbæk (2016) studied rot in spruce in higher altitudes of eastern Norway and found results that contradict the notion of *H. parviporum* as the most prevalent fungi in spruce at higher altitudes. The study areas ranged from an altitude of 585 – 840 meters above sea level. The results revealed that 32.8% of the stumps contained rot. *Armillaria spp* 38.9% was most frequent, but only 7.2% was caused by *H. parviporum*. This study shows that even though *H. parviporum* is considered the more dominating fungus in spruce, this may vary with altitude, and the occurrence of *Armillaria spp.* may be more dominating in some cases. Furthermore, the results also included numerous lesser-known and unidentified species of fungi that occurred more frequently compared to *H. parviporum*. Even though *H. parviporum* and *Armillaria spp.* are considered as the dominant fungi in spruce, the results show a more complicated picture. The dominant fungi may vary with local conditions and other factors. Still, enough evidence remains to support *Heterobasidion spp.* and *Armillaria spp.* as the two dominant fungi to cause root and but rot in spruce in eastern parts of Norway.

Biology of *H. parviporum* and *Armillaria spp.*

H. parviporum spreads in one of two ways, known as primary- and secondary spread (Solheim, 2010). Primary spread happens through spores carried by wind, water or birds to freshly cut stumps, or wounds in the tree, where it can induce an infection. Freshly cut stumps have shown to be ideal for spores to establish within a limited time frame depending on competition from other fungi, temperature, moisture and spore production (Redfern & Stenlid, 1998a; Solheim, 2010). Secondary spread develops through root contact, or grafts, between infected and healthy trees where the mycelium is transferred (Solheim, 2010). Infection through root contact becomes more important for further spreading as the forest ages, and usually occur in conjunction with thinning and final felling where it spreads to new trees (Molin, 1957; Redfern & Stenlid, 1998b). Areas with frequent root death, caused by unstable groundwater conditions or other reasons, are more receptive to infections. Typical soil conditions where rot recurs are calcareous and nutrient-rich soils and arable lands (Solheim, 2010). Some studies also show a higher tendency for rot within areas with limestone and high pH values (Korhonen & Stenlid, 1998). Young infected trees usually die within 3 years. In older trees, the rot is chronic and develops internally. The rot expands both vertically and horizontally, and can reach heights

beyond 12 meters (Solheim, 2010; Stenlid & Wästerlund, 1986). As a white-rot fungus, it gradually decays the cellulose in the wood, leaving behind a soft wood texture where it has established itself (Solheim, 2010). The rot can also affect the growth in addition to the quality. Bendz-Hellgren and Stenlid (1995) found that the diameter increment was smaller for infected trees compared to healthy by 10.1% over 10 years. A later study by Bendz-Hellgren and Stenlid (1997) supported these findings. Infected and healthy trees were paired and monitored for over 4 years. A comparison showed a reduction in volume growth by 23% for the infected trees.

Like *H. parviporum*, *Armillaria spp*. also spreads by spores and through root contact. As the rot develops in an infected tree, it starts to produce rhizomorphs, which grows through the forest floor and connects to new roots where it can prompt new infections. Infection through rhizomorphs usually happens in damaged, weakened or dead roots, and is considered more important than spores for infection. Stressed trees are more exposed to infection (Solheim, 2010). The fungus is less aggressive and mostly remains in the heartwood where it gradually advances. Heights beyond 1-2 meters in the stem have rarely been observed (Solheim, 2006). In addition to cellulose, it also consumes lignin, destroying the wood that is affected. Once infected, young trees commonly die within 2 years, while the process takes a longer time in older trees. As the infection advances the crown commonly turns yellow and the shoots become shorter. In the end, the tree can die from the top (Solheim, 2006).

Existing methods to detect rot in standing forest

The life cycle of *H. parviporum* and *Armillaria spp*. illustrates how these fungi can have such a financial impact in the forest sector. Both mostly develop internally and few external symptoms are visible (Redfern & Stenlid, 1998b; Solheim, 2010). In cases where the rot has advanced significantly, the crown can be reduced and the needles start to turn yellow (Greig, 1998; Huse et al., 1994). This can also be the result of multiple other circumstances like drought or attacks from pests, making it hard to determine the exact cause (Hanssen et al., 2019). Moreover, they establish themselves at the center at the bottom of the stem, where the wood is gradually decayed. This is where the largest industrial potential is, and decay can render this part useless in an industrial context. Additionally, *H. parviporum* and *Armillaria spp*. can survive as saprobic organisms in dead trees for a long time. In the remaining stumps and roots after final-felling, *H. parviporum* can remain contagious for 50 years and possibly infect new trees and cycle rotations (Solheim, 2010).

Given that the rot shows few visible external symptoms in trees, it is hard to detect it without using destructive measures (Carson et al., 2006). There are developed methods for rot detection, but these are carried out manually on individual trees. This can either be done by taking a core sample or using specially developed tools. Core samples are often taken at breast height (1.3 m). The sample is then inspected to determine whether the tree is infected by rot (Carson et al., 2006). Since the samples are taken at a specific height, this might cause the method to underestimate the amount of rot, since it can be present at lower heights that are not inspected (Huse et al., 1994). Several specially developed tools use non-destructive methods. The use of ground-penetrating radar and ultrasounds are common for these tools (Carson et al., 2006). Rotfinder is an example of a tool specifically developed to detect rot in trees using a non-destructive method by applying an electric current to the tree. Based on the resistance, this tool can distinguish between healthy and infected trees (Larsson et al., 2004; Sundblad et al., 2008).

Information regarding rot occurrence is essential in forest management. A forest inventory including this information can be presented as a map and contribute to strategic choices. This could result in a better economic outcome for the forest owner if used to take measures that reduce the negative effects of rot. The existing methods to gather this information are currently inefficient. The methods are time-consuming and performed manually on individual trees. Rot can affect large areas within the forest, but the prevalence might not be that high. Hence, with the methods currently available, inventory of large forest areas would require extensive resources to get a clear picture of rot prevalence. The lack of distinct symptoms presents a challenge and prompts the development of new methods that can detect rot over large areas with high accuracy (Leckie et al., 2004).

Airborne hyperspectral images and laser scanning
The method of using remote sensing to collect information is a promising candidate that could detect rot over large areas with high accuracy. Remote sensing is the collection of information about an object without the need to be in direct contact with the object you are examining (Lillesand et al., 2008). Airborne hyperspectral and laser scanning instruments are remote sensing sensors capable of registering information about objects over large areas.

Hyperspectral sensors can register highly detailed data with spectral information. Normally, a picture is constructed of multiple pixels where each pixel contains a singular value (e.g. color). In a hyperspectral image, each pixel contains multiple radiance values in addition to spatial information (Grahn & Geladi, 2007). Each value represents the reflected electromagnetic energy in distinctive wavebands across the electromagnetic spectrum. The number of wavebands, and scope of the electromagnetic spectrum where data are gathered, depends on the sensor used. Multispectral sensors are also capable of registering spectral data, but they often register values in 3 to 12 wavebands. Hyperspectral sensors generally have over 100 wavebands. This means that each pixel contains over 100 unique radiance values. The increased level of detail enables the detection of small differences in objects which multispectral sensors may not be able to differentiate (Adão et al., 2017). Hyperspectral sensors are in constant development, and new sensors are expected to arrive with greater spatial and spectral accuracy. A pixel from a hyperspectral image can be illustrated as a cube (see figure 1). The spatial information is registered in the x-axis and y-axis. The z-axis represents wavelengths from the electromagnetic spectrum. The scope of the electromagnetic spectrum analyzed, and how many wavebands the spectrum is split into, varies depending on the sensor used. Hence, a pixel consists of numerous layers of wavebands along the z-axis with radiance values registered in each waveband.
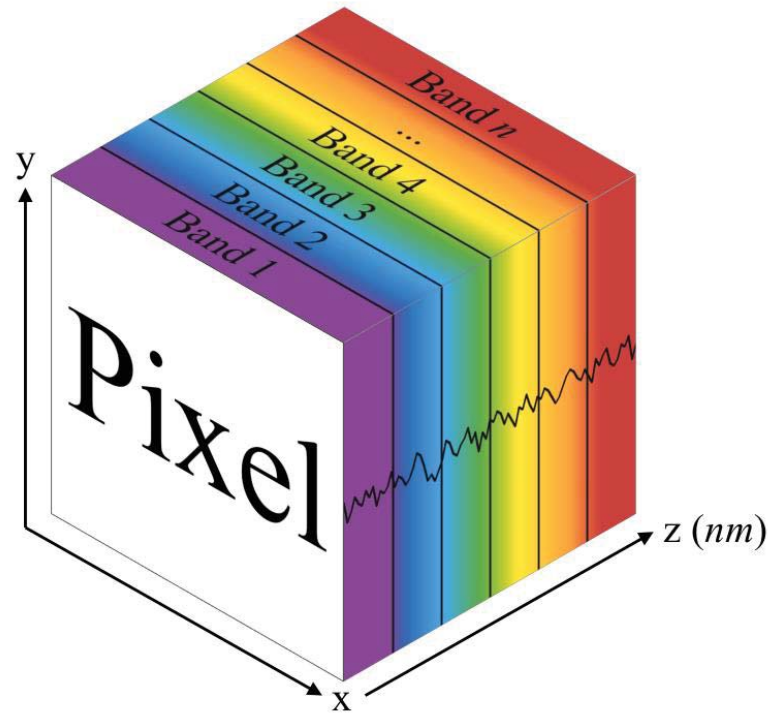
Figure 1: Illustration of a pixel from a hyperspectral image. Spatial information is registered in the x-axis and the y-axis and spectral information is registered in the z-axis.

Airborne laser scanning (ALS) is a remote sensing method using a laser scanner mounted in an aircraft and connected to an inertial navigation system and a global navigation satellite system (GNSS). The sensor distributes laser light in pulses and can register millions of points per second. Each point is georeferenced and attributed value for height. This is made possible by calculating the duration from a laser signal is emitted until it gets a reflected signal in return. The result is a point cloud from which it is possible to create digital models of the earth's surface. Terrain and vegetation points can be classified. Vegetation points can be further processed to separate individual trees and give information about the physical properties of the forest. This gives ALS multiple applications within forestry (Maltamo et al., 2014). Figure 2 demonstrates how a laser sensor attached to an airplane maps the earth's surface.
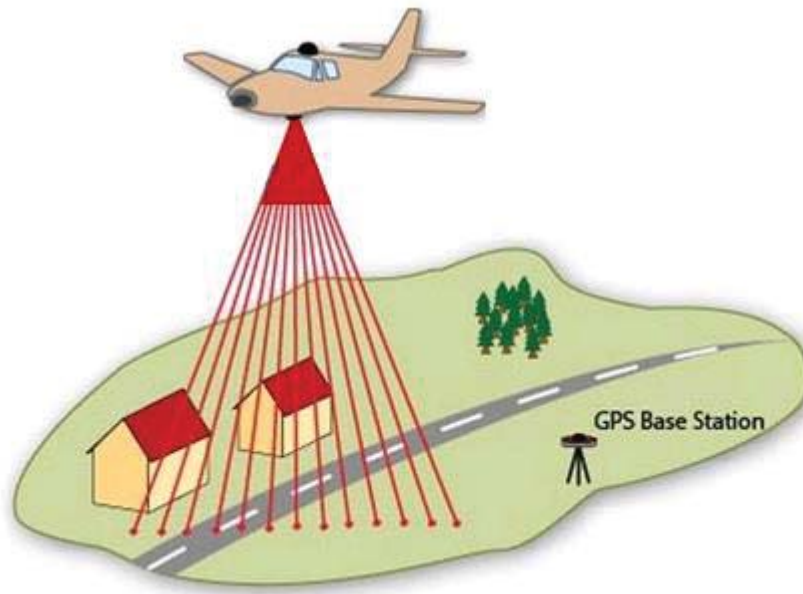
Figure 2: Illustration of airborne laser scanning (University of Connecticut, n.d.)

Historically, forest inventory has been based on manual measurements in the field combined with the interpretation of aerial photos. This has gradually been replaced by ALS, which has been common in Norway since the early 2000s (Kangas et al., 2018). The use of ALS has proven to be a cost-effective alternative able to cover large areas (Eid et al., 2004), and has become the most applied method in the collection of data and information in forest inventory (Solli et al., 2013). The use of ALS serves multiple purposes in forest inventory and is commonly used to collect quantitative information about the physical properties of a forest (e.g. dominant height of trees in a stand). The spectral signature of a tree is affected by its physical characteristics. Therefore, hyperspectral images facilitate the possibility to obtain information about the biophysical properties of the forest. Multiple studies have done this and show promising results. Hyperspectral images have been used to reveal information about tree's water management, plant health and stress factors (Kandare, 2017; Moorthy et al., 2008; Thenkabail et al., 2013). The combination of ALS and hyperspectral images presents the potential for multiple uses that could benefit forest management (Kandare, 2017). Anderson et al. (2008) looked at the individual and combined use of ALS and hyperspectral imagers to estimate biophysical properties. Combined, they gave the best results. Kandare et al. (2017) used a combination of ALS and hyperspectral images to estimate site index at various special scales including individual trees, and the approach showed promising results. Bollandsås et al. (2019) study on modeling of site index using hyperspectral images substantiates these findings. Hyperspectral imagers alone proved to be efficient at predicting site index, but the inclusion of

ALS further improved the model. Sørhuus (2019) used hyperspectral images to detect rot in spruce. His models were based on analysis of a single pixel per tree from hyperspectral images. The study displayed encouraging results but concluded with the need for more pixels to develop better models. Based on the existing research in the field, the combination of airborne hyperspectral images and laser scanning show potential as an accurate and cost-effective method to detect rot over larger areas with high accuracy.

Thesis objective

As society continues to increase its use of renewable resources, forest management must be given better tools that contribute to more efficient management of the available resources within the forest. Researchers predict further damage from rot with pending climate changes. The existing methods to detect rot over larger areas are inefficient and promote the need to develop new methods.

The objective of this thesis is to explore if the combination of airborne hyperspectral images and laser scanning can be used to identify root and butt rot in Norway spruce with high accuracy. The study builds on previous research and applies state of the art remotely sensed data.

Material and methods

Workflow

A workflow describing the process of this study is illustrated in figure 3. Each step of the workflow and the dataset analyzed in this study are presented in the following subsections.
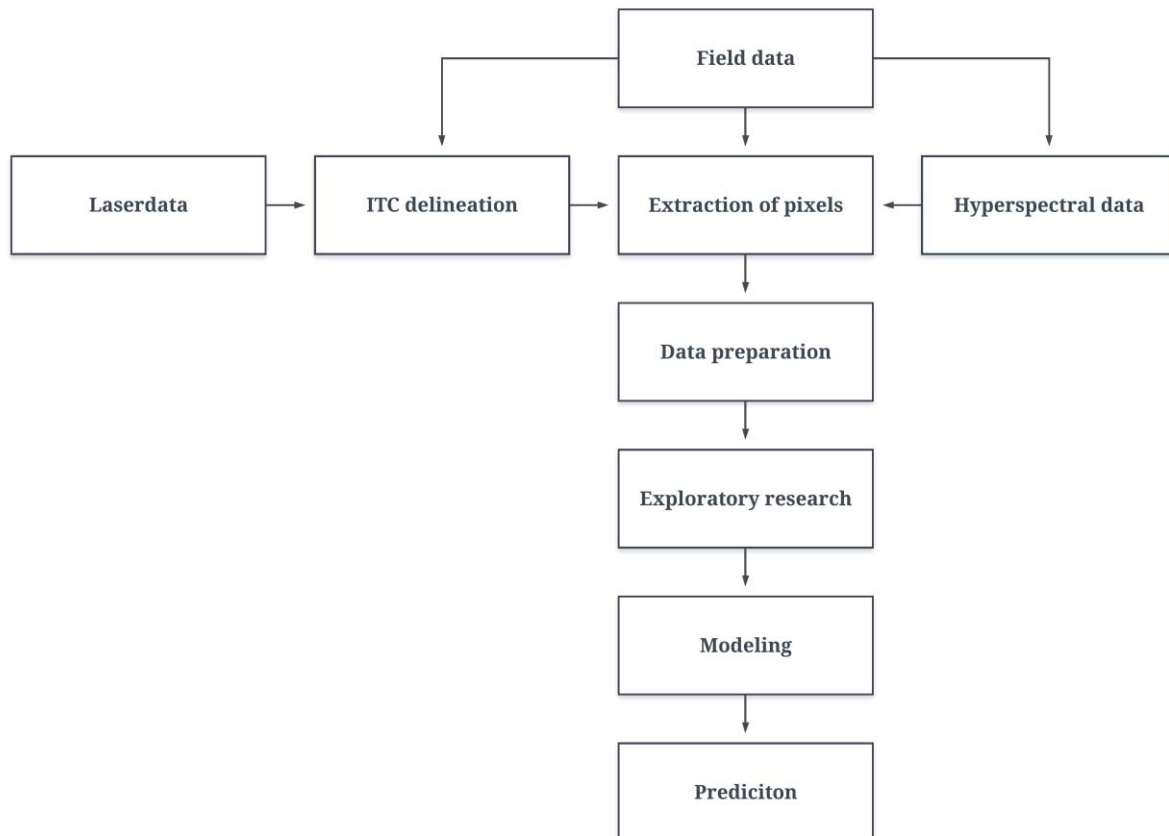
Figure 3: Workflow illustrating each step in the process of this study.

Study area

The study was conducted in south-east Valdres close to the village Bruflat, in Etnedal municipality in Innlandet county. The study was conducted in one location (see figure 4) at an altitude of 700 meters above sea level. The area consisted of 3 different spruce stands with spruce (95%) as the main tree species along with pine (5%). The age of the different stands ranged from 81-131 years and the size of the stands varied from 0.45-7.75 ha. The total size of the area is 9.23 ha. The information about the stands was extracted from a forest inventory carried out in 2008 and the properties can be seen in table 1. The main data collection was performed in stand 1. The road passing the study area was constructed during the stands cycle.
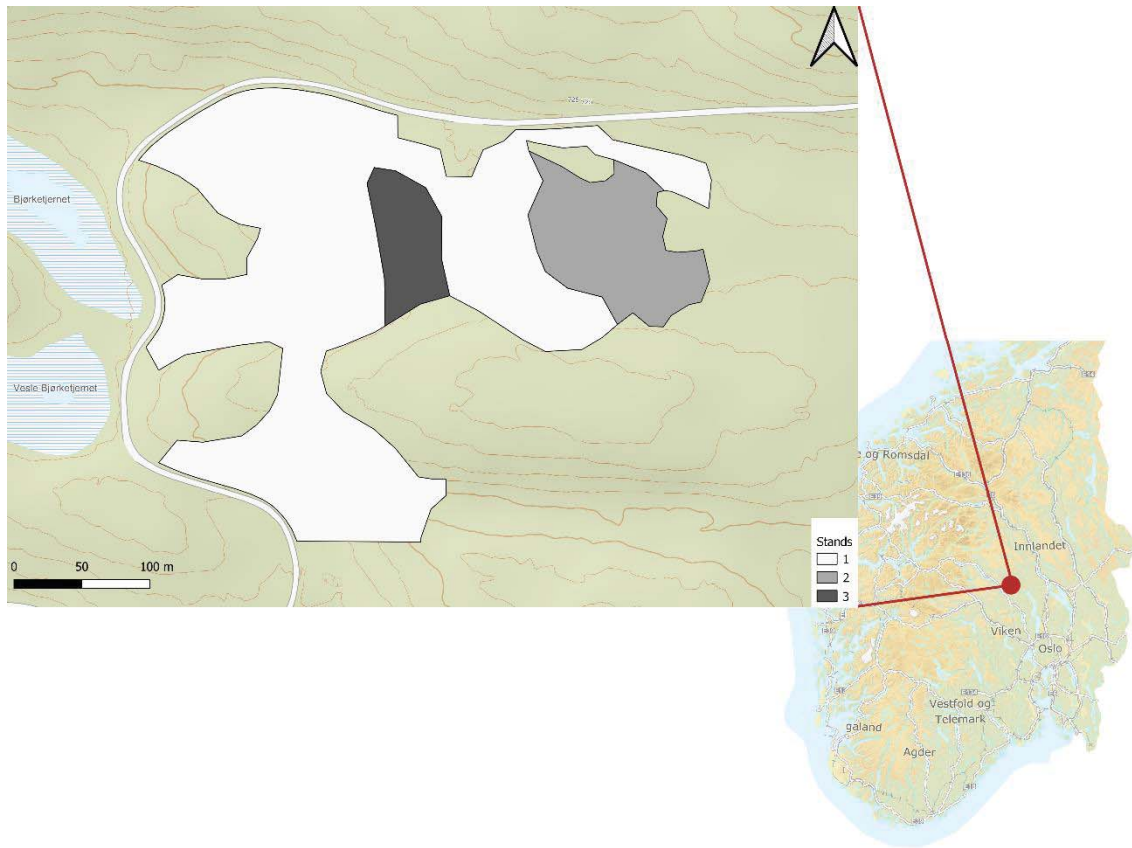
Figure 4: Overview map of the study area in Etnedal municipality.

Table 1: Stand data from the study area in Etnedal municipality.

Stand	Distribution (S/P) [1]	Site index[2]	Age
1	95/5	11	131
2	100/0	11	91
3	90/10	11	81

[1]Composition of tree species in the percentage of total volume, S = spruce, P = pine.

[2]Site index (H_{40}): defined by average age at breast height and the average height of the 100 largest trees per hectare according to the diameter at breast height (dominant height) and where the specific values of the H40 index relate to the dominant height at an index age of 40 years (Tveite, 1977).

The geological data about the study area are presented in table 2 (Geological survey of Norway (2015).

Table 2: Geological description of the soil and bedrock in the study area (Geological survey of Norway (2015).

Soil	Bedrock
Moraine: incoherently or thin cover over the bedrock	Sandstone: sand-sized mineral particles, quartz and feldspar.

Data collection

The data were collected in week 38 in September 2019. The data consist of two sets. The first set was in collaboration with another study and contained only stumps where rot was already selected (Moen, 2020). The stumps were spread out over the entire study area. The registrations were done during the two previous weeks. Core samples were taken at root cut and examined for rot. Based on the core samples, trees that were suspected of being infected by rot were singled out for further inspection before final felling was carried out. During harvest, each stump of interest was visually inspected for rot. Stumps with rot were then marked and given an ID, and their GNSS position registered. The GNSS positions registered using the harvester performing the cutting were expected to have a mean error of less than 1 m and were used to locate the stumps for the data collection in this study.

The second set of data was collected using strip sampling. Each strip was laid out as a straight south-north line and had a width of 3 meters and a space of 10 meters between them. Since the data collection was time-consuming, the strips were distributed to cover most of the different terrain in the study area. Additionally, there were multiple cases where stumps occurred in both data sets. These were registered as duplicates.

Only stumps of spruce trees were included in the registration. Each stump was marked and given a tree ID which corresponded with the GNSS point registered, visually inspected for root and butt rot, and registered as healthy (no rot) or infected (rot). If the stump had rot, this was classified as either *H. parviporum*, *Armillaria spp.* or other. The diameter of the stump and the rot was cross measured with a caliper in north-west and north-east directions. For each stump, the position was also registered with a TOPCON HiPer SR (Topcon, n.d.). This is an extended range site receiver with GNSS and RTK (Real-Time Kinetic). The receiver includes GPS (Global positioning systems), GLONASS (Global Navigation Satellite System) and a cellular modem for real-time correction of positioning. The correction data were obtained from the CPOS service at the Norwegian Mapping Authority (2017). Each registration was done in a

fixed position at the center of the stump. The horizontal root mean square ranged between 1 – 3 cm and the average was 2 cm. This is the error of margin for the positioning of each stump. All the stumps were also photographed with an Olympus TG-5 camera with GPS-positioning built-in. This was done in order to secure information that could be utilized later if the data needed correction or to be controlled.

There were 318 samples in total. The number of samples was later reduced to 274 before further analysis after removing duplicates and stumps from the first dataset which were corrupted during harvest and made visual inspection impossible. Of the 274 samples, 112 were classified as healthy and 162 as infected trees. The positions of the stumps can be seen in figure 5.
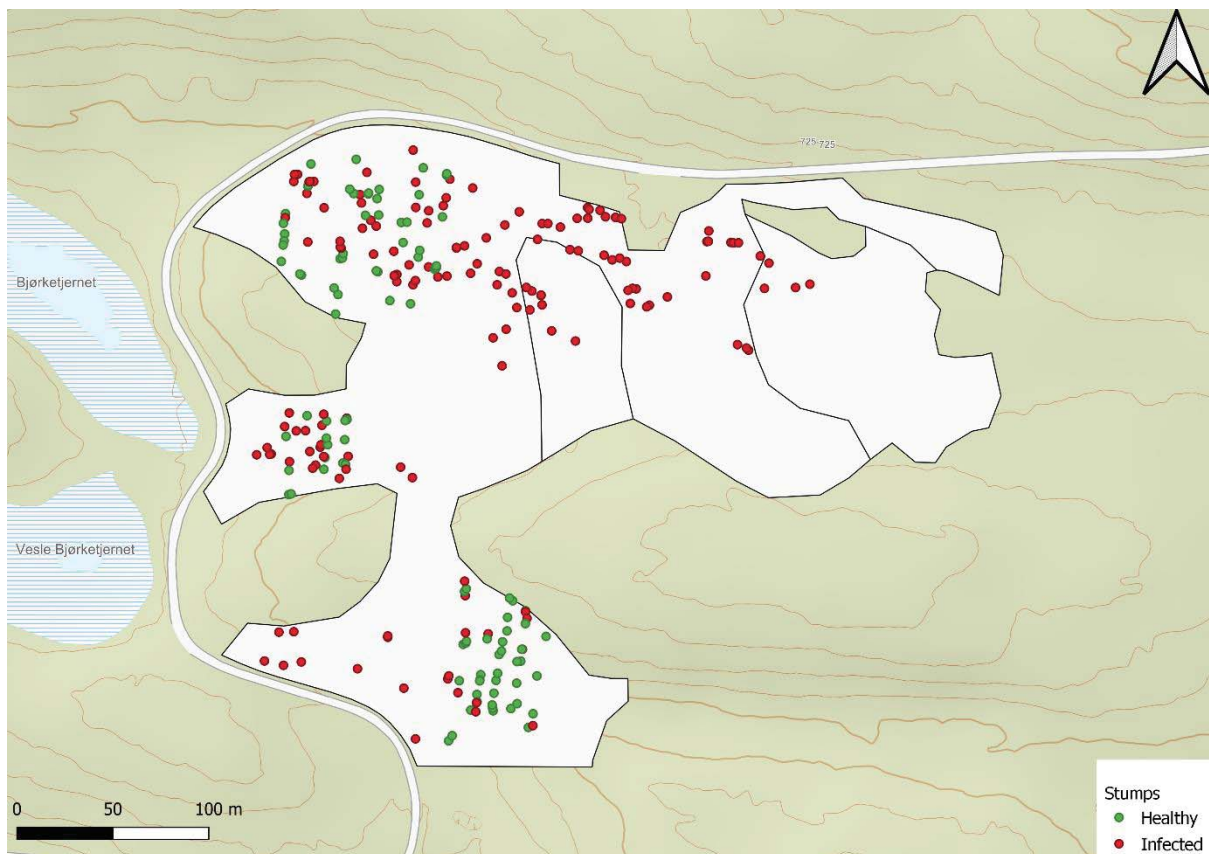
Figure 5: Registered stumps showed as healthy (green) or infected (red).

Collection of airborne hyperspectral images and laser scanning data

The airborne hyperspectral images and ALS data were collected on 03.08.2019 by Terratec AS (n.d.). The airplane used was a Piper PA-31-350 which carried two HySpex sensors capable of taking hyperspectral images: VNIR-1800 and SWIR-384 which were mounted in a gyro frame. These cameras collect data in the visible near-infrared, and the short wave infrared, spectral

range (HySpex, n.d.). The cameras were calibrated after parameters given by Norsk Elektro Optikk AS, the company developing the cameras (Norsk Elektro Optikk AS, n.d.). The specifications of the cameras can be seen in table 3. The hyperspectral data contains georeferenced hyperspectral images with a resolution of 0.3×0.3 meters for the VNIR camera and 0.7×0.7 m for the SWIR camera. Each pixel in the image contains multiple channels with information from the spectral range.

Table 3: Specifications for the hyperspectral cameras used in this study (HySpex, n.d.).

Sensor	VNIR-1800	SWIR-384
Spectral range	400-1000 nm	930-2500 nm
Spatial pixels	1800	384
Spectral channels	186	288
Spectral sampling	3.26 nm	5.45 nm
Field of view (FOV)	17°	16°
Pixel FOV across/along	0.16/0.32 mrad	0.73/0.73 mrad
Max speed at full resolution	260 fps	400 fps

In addition to the hyperspectral images, laser data were collected with the Leica ALS70-HP ALS (Leica Geosystems AG, n.d.). The laser scanner creates georeferenced points with height attributes. The settings the ALS used during data collection are presented in table 4.

Table 4: Settings for the airborne laser scanner used in this study.

Measurement rate (kHz)	495.2
Field of view (FOV)	16°
Scan patters	Single
Scan rate (Hz)	68.9

The aircraft maintained an altitude of 1150 meters and had a maximum speed of 130 km/h during data collection. The data was processed by Terratec. The georeferencing was performed with nearest neighbour interpolation in PARGE 3.4 (ReSe, n.d.). Corrections of heading, roll and pitch were performed by manual selection of natural control points between two crossing flight paths.

ITC delineation

To delineate ITCs from the laser scanning data provided by Terratec for the study area, the itcSegment package (Dalponte, 2018) version 0.8 was used. The laser scanning data consisted of a raw point cloud where each point has height registered. By analyzing the variation in heights, the algorithm creates a canopy height model (CHM) where treetops are identified. The algorithm then proceeds to grow tree crowns outwards from the identified treetop according to parameters defined by the user. This process repeats itself for all identified treetops resulting in polygons that represent individual tree crowns (ITCs). Figure 6 shows a portion of the study area with ITCs as polygons in green. The default input parameters were used in this study.
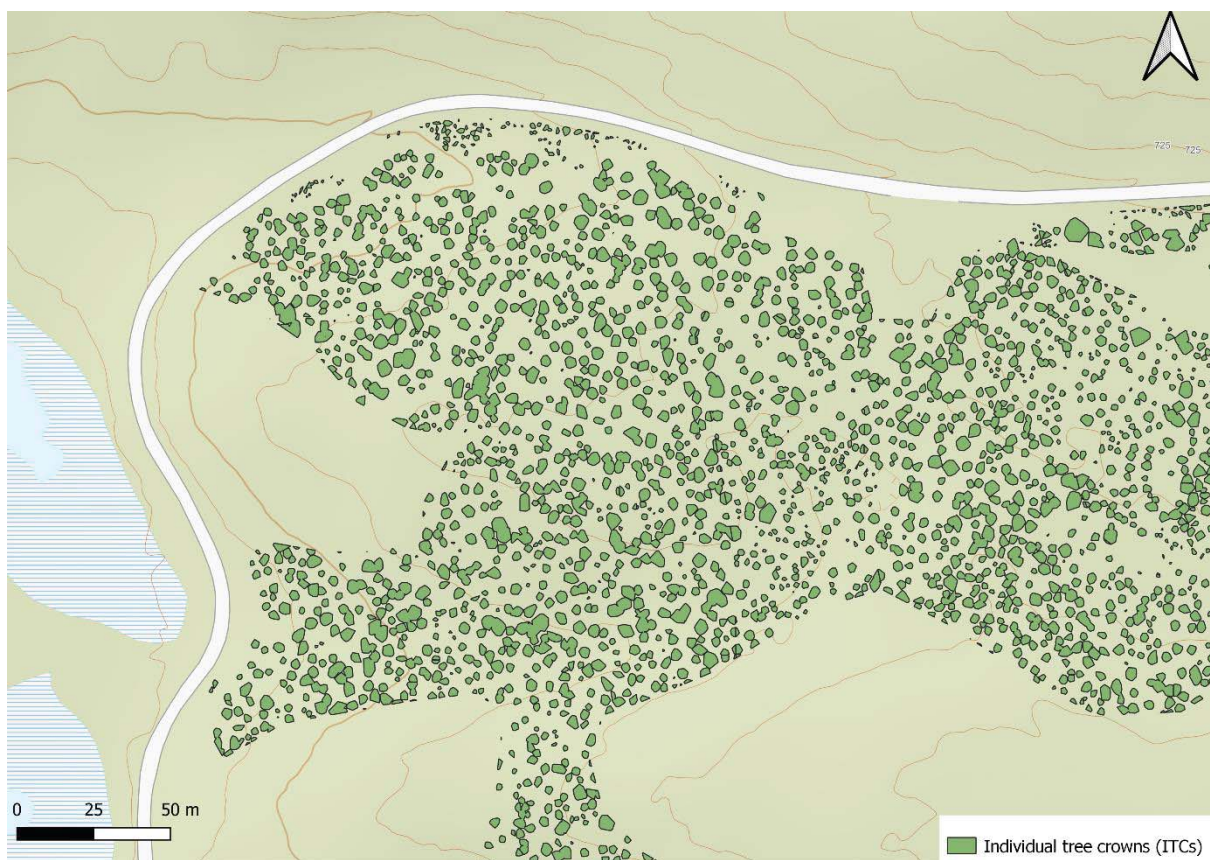
Figure 6: Polygons representing individual tree crowns (ITCs) calculated from the delineation algorithm.

Preparation of data

The ITC polygons were further processed in QGIS Geographic Information System (2020) to extract the hyperspectral data used for analysis and modeling. To single out the individual trees where field data had been registered, polygons with corresponding GNSS points from the data collection were isolated. A few GNSS points did not have a corresponding ITC polygon, and these were removed from the dataset (n = 26). Furthermore, some polygons contained several

16

GNSS points, indicating that some of the polygons were wrongly delineated to a single tree. Trees positioned close together could explain this phenomenon. To correct this, Voronoi polygons were created around GNSS points. A Voronoi diagram divides the plane into regions where all the points within individual regions are closest to a specific object. In this case, the GNSS points were used as the input to divide the plane using the Voronoi polygons. From the Voronoi polygons, the ITC polygons were split and matched with the GNSS points. Subsequently, some of the polygons were split into several parts, even though they only contained one GNSS point. This happened in areas were polygons were closely related to each other. To amend this problem, the polygons were manually inspected and corrected, and the final number of polygons were controlled and matched with the number of remaining GNSS points. A subjectively selected subset of the result can be seen in figure 7.

Figure 7: Split ITC polygons as a result of the Voronoi diagram.

To simplify the data processing in R, the SWIR images were resampled to the same resolution as the VNIR image (1960 × 1295) with a pixel size of 0.3 × 0.3 m. A nearest neighbor method was used during the resampling. This ensures that both images have the same number of pixels with information for statistical analysis and modeling. The ITCs polygons were converted from

vector to raster with the same resolution as the hyperspectral images preserving the tree ID information in each pixel. The tree ID was stored in order to distinguish individual trees and to classify the pixels as either healthy or infected. Lastly, the ITC raster was merged with the hyperspectral images from VNIR and SWIR before being imported into R.
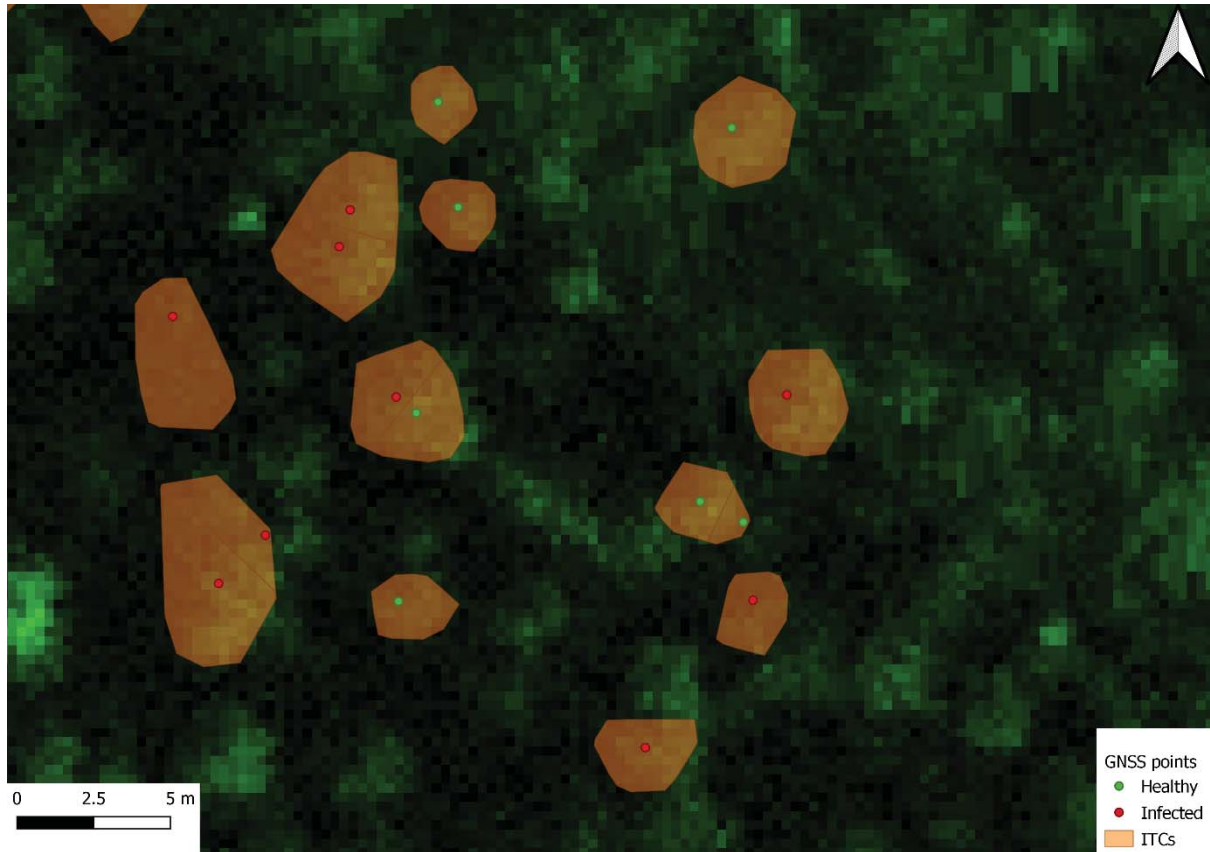
Figure 8: Illustration of how ITCs were used to extract pixels from the hyperspectral images. The image in the background is from the VNIR sensor.

Further preparation, analysis and modeling were computed in R (R Core Team, 2020) version 4.0.0. All the extracted pixels were grouped after tree ID and assigned a corresponding value for the state (healthy or infected) using the ID as an identification key. All pixels with the same tree ID constituted a single tree. After removing GNSS points with missing ITC polygons, 248 trees remained where 96 were healthy and 152 were infected. The number of pixels per tree varied from 7-226, and the average amount of pixels per tree was 71. The total amount of pixels extracted was 17.718. Each pixel contained information from both sensors with a single value for light intensity (radiance) in distinctive wavebands. This amounts to 8.4 million radiance values as the basis for data analysis.

Pixels in the hyperspectral images can suffer from a shadow effect causing inaccurate radiance values. This is especially a problem at northern latitudes with shadows present even during optimal acquisition periods (Dalponte et al., 2014). This was not accounted for in the dataset from Terratec. Some combinations of wavelengths have proven useful in distinguishing vegetation and characteristics of vegetation. This knowledge can be used to clean up the dataset by implementing a normalized difference vegetation index (NDVI) (NASA Earth Observatory, 2000). The index uses wavelengths from the near-infrared and visible red spectrum, and NDVI was calculated after formula (1) using wavelengths 810 nm for NIR and 680 nm for RED (Ju et al., 2014). The formula returns a value between 0 and 1 which can be used as a basis for selection. Pixels with an NDVI score < 0.6 often contain aspects of shadow or other elements (Kandare, 2017) and was used as the threshold for removal. Clean up of the dataset using NDVI resulted in the removal of 4.263 pixels.

$$(1) \; NDVI = \frac{(NIR - RED)}{(NIR + RED)}$$

After removing pixels with NDVI, the data was normalized. The goal of normalization is to reduce the data to a common scale without distorting the differences in the ranges of values and to improve the integrity and performance of the models. Since the accuracy of hyperspectral image classification can be affected by the chosen normalization method, several different methods were considered (Cao et al., 2017). Based on Cao et al. (2017) comparisons of different normalization methods for hyperspectral image classification, the data were normalized after formula (2). The normalized radiance value x_{ij}^* is a result of the original radiance value x_{ij} divided by the maximum radiance value $bandmax\,(x_{ij})$ identified from all registered radiance values in the distinctive wavelength.

$$(2) \; x_{ij}^* = \frac{x_{ij}}{bandmax\,(x_{ij})}$$

Exploratory research

Before modeling the data, a preparatory exploration of the data was executed to see if individual wavebands in the electromagnetic spectrum could show any significant differences between healthy and infected trees. As a precursor, the mean radiance values for healthy and infected trees along all wavelengths were plotted to see if there were any significant differences

between them. To examine the significance of the different wavebands, Welch's t-test was performed on individual wavebands from the NVIR and SWIR datasets. A total of 474 t-tests were completed across both. P-values below 0.05 were considered significant for the t-tests. A closer inspection of the dataset from SWIR revealed a lot of noise in radiance values in wavelengths above 1800 nm. This was caused by missing values or values close to 0. The t-test results from these wavelengths were therefore disregarded in the evaluation.

After the preparatory examination, the data was split into two datasets (see table 5). One dataset contained all the radiance values and the second dataset contained the mean waveband radiance values aggregated based on tree ID. This was done to see if there were any statistical difference between analyzing all and mean radiance values (i.e. multiple, or one radiance value per tree per waveband).

Table 5: Difference in datasets size of all and aggregated radiance values.

Dataset	Total number of radiance values
All radiance values	6.377.670
Aggregated radiance values	117.552

Prediction models

A dataset with known classifications is fundamental in the development of prediction models. Based on a training dataset, prediction models can be developed which can predict classification on new data with equivalent variables. Normally, a dataset is split into a training and validation set before the model is fitted. Since the validation dataset includes true classifications, this can be used to evaluate the performance of the predictions made by the model. Logistic regression and random forest models were fitted to the data. To enhance the performance of models, only data from distinctive wavebands based on results from Welch's t-tests were included. Both models were fitted with all and aggregated radiance values separately. Before modeling, the data were split into healthy and infected trees. From the split datasets, 10 random samples were taken in an 80/20 ratio and reassembled for training and validation sets. The data was split before they were designated to training and validation sets to ensure all random samples included an equal amount of healthy and infected trees when fitting the model. Both models were then fitted with the 10 different samples. For all individual models, the 15 most significant wavebands and their wavelengths were extracted to see if there

were any correlation in the models. The selection was based on P($>$|z|) for the logistic regression models and mean decrease accuracy for the random forest models. The goal of the prediction models is to find the variables that best distinguishes between healthy and infected trees with high accuracy. The best model can then be used to predict the classifications of new trees.

Logistic regression

StepAIC from the MASS package (Venables & Ripley, 2002) version 7.3.51.6 was used for the logistic regression model. The model was adapted with a combination of forward and backward variable selection. In each step, the model can both include and remove variables. From this process, numerous models are adapted and the Akaike information criterion (AIC) is calculated. AIC is a measure of the quality of the model and provides a medium for model selection from which each model is compared relative to each other (Wang et al., 2013). By repeating these steps, the algorithm tries to simplify the model to include the optimal variables to explain the variations in the dataset. The result is a logistic regression model combined of selected wavebands which best predicts classifications of trees.

Random forest

To compute the random forest model, the randomForest package (Liaw & Wiener, 2002) version 4.6.14 was used. Random forest is an ensemble learning method. From a dataset, the algorithm takes random samples to grow numerous relatively uncorrelated decision trees for prediction. The process of repeated random sampling is known as bootstrapping, and the process repeats itself until a defined number of trees have been grown. When given new data, all the decision trees in the model make a prediction based on the input. The prediction follows a path of nodes that resemble crossways. In each node, the variables are compared and matched with accumulated knowledge. At the end of the path, a prediction is made based on comparisons made along the way. Collectively, each decision tree gives its own prediction, but the sum of all their predictions gives the final classification (see figure 9). Hence the definition as an ensemble method. The process of growing multiple trees from the same training dataset ensures the model can make precise predictions to assist in the classification of new trees (Suthaharan, 2016). In this study, the model was set to grow 500 decision trees per dataset.
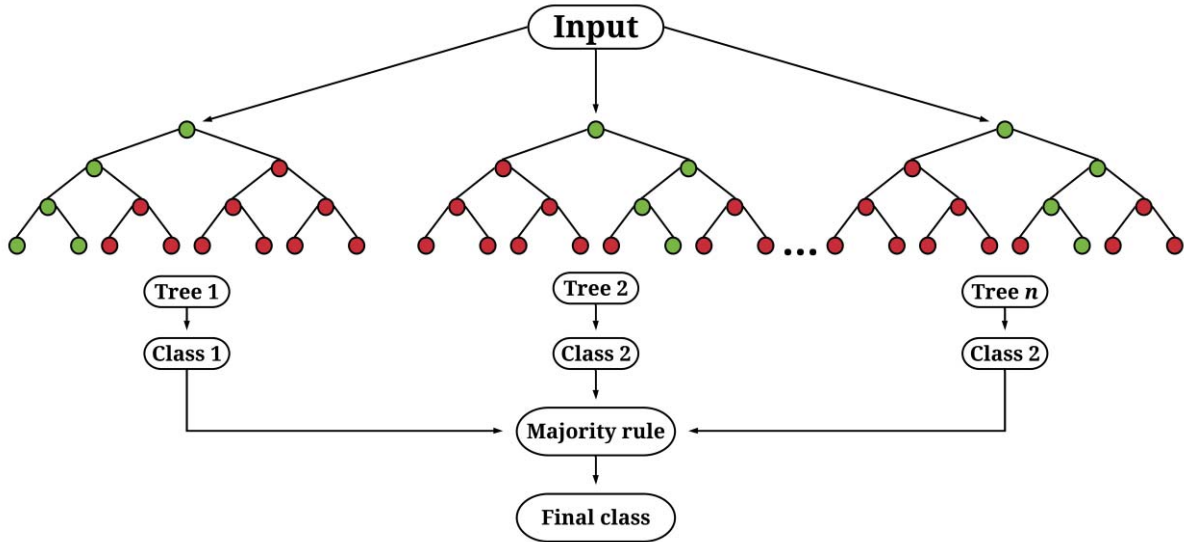
Figure 9: A simplified example of how a random forest model makes a prediction. Each decision tree makes its individual prediction, then the final classification is based on majority rule.

Model validation

For each model, mean prediction accuracy, Cohen's kappa and area under the receiver operating characteristic curve (ROC) were calculated and used as an aid in model validation. Mean prediction accuracy expresses the proportion of correctly classified trees in a model. A tree can be classified as healthy when it is infected and vice versa. This gives four possible outcomes: true positive, false positive, false negative and true negative, where only two are classified correctly. The logistic regression model is dependent on a threshold to determine a classification from the predictions made. In this study, the threshold was set to 0.5. Each prediction gives a numerical value for probability between 0-1. If the returned value is < 0.5 it is classified as healthy, and values > 0.5 are classified as infected. After all the predictions from a model had been made, the results were collected in a confusion matrix. Here the results from the four possible outcomes are displayed as a table that can be used to describe the performance of the model in terms of mean prediction accuracy.

The confusion matrix is also essential in the computation of various statistical goals for compliance in prediction models and facilitates the calculation of Cohen's Kappa. This coefficient expresses the reliability between the observed and predicted classes and permits the interpretation of the compliance among them. A numerical value between -1 and +1 is obtained from Cohen's Kappa, where +1 is the ideal reliability. The method acknowledges unpredictability and considers this for the results of singular classifications (McHugh, 2012).

The last parameter used for model validation was the area under the ROC curve. The area under the ROC curve takes classifications of true positives and plots these against false positives. The area under the curve is estimated and given a number ranging from 0.5-1. The result expresses the model's ability to discriminate between healthy and infected trees. If the area is 0.5, there is an equal amount of illegitimate and legitimate classifications (Chrzanowski, 2014).

Results

Overview

The VNIR sensor contains radiance values from wavelengths between 400-1000 nm. The largest difference between healthy and infected trees occur between 750-900 nm (see figure 10).

Figure 10: Mean radiance values and standard deviation for healthy and infected trees in all wavelengths between 400 – 1000 nm. The data is from the VNIR sensor. Healthy trees are displayed as green and infected as blue.

The SWIR sensor contains radiance values from wavelengths between 930 – 2500 nm. The largest difference between healthy and infected trees occur between 1000 – 1025 nm, and between 1200-1300 nm (see figure 11).
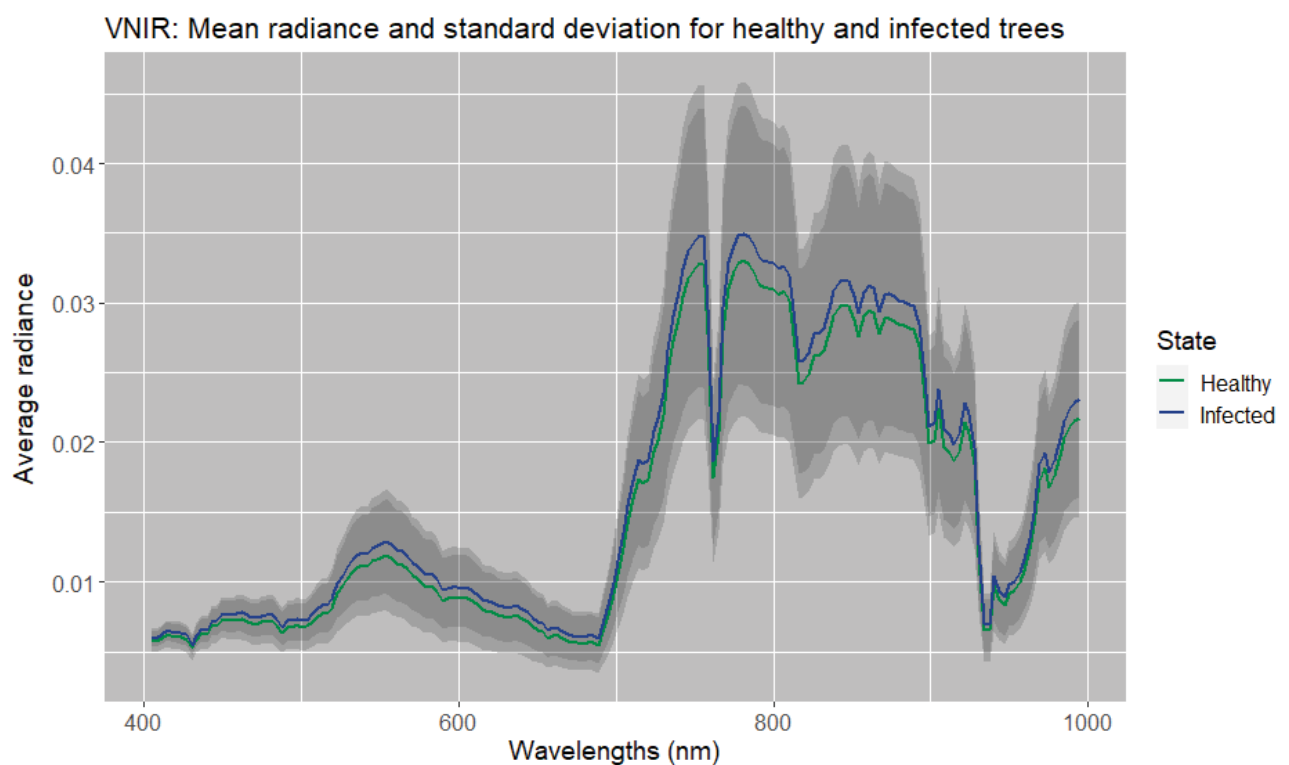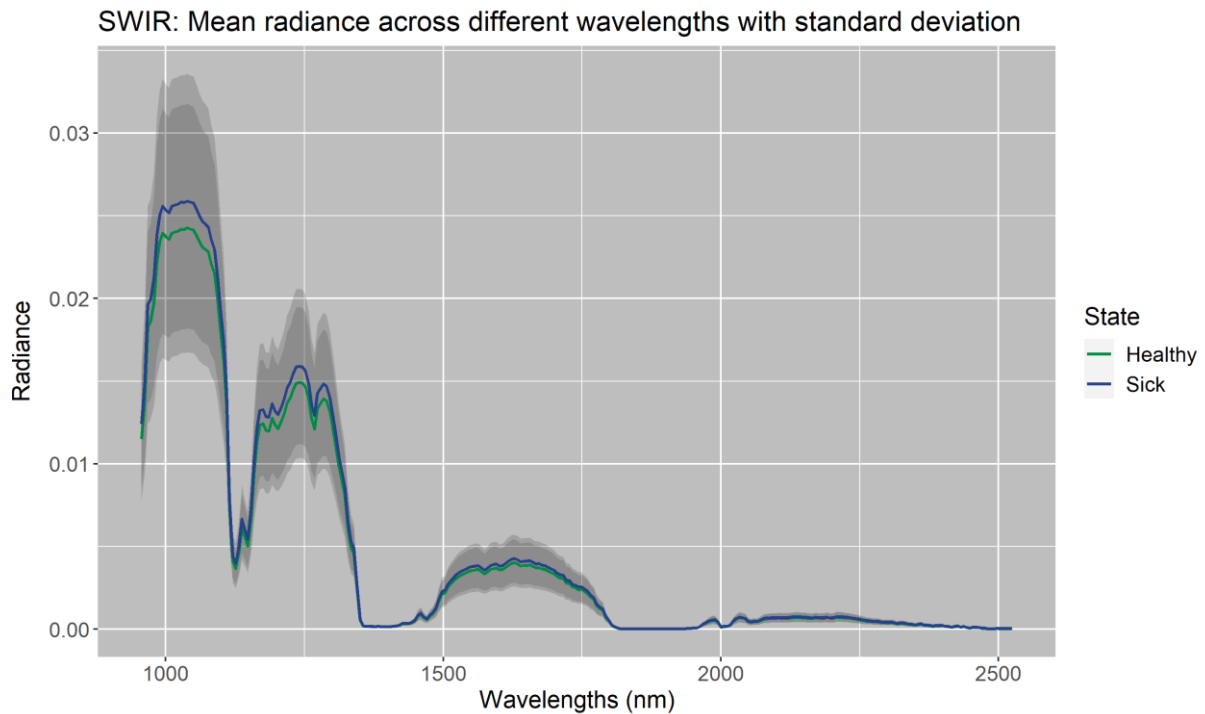

Figure 11: Mean radiance values and standard deviation for healthy and infected trees in all wavelengths between 930 – 2500 nm. The data is from the SWIR sensor. Healthy trees are displayed as green and infected as blue.

Welch's t-test

For the VNIR dataset, significant values (p-value < 0.05) were detected in wavelength intervals between 405-526 nm and 575-669 nm (see figure 12).
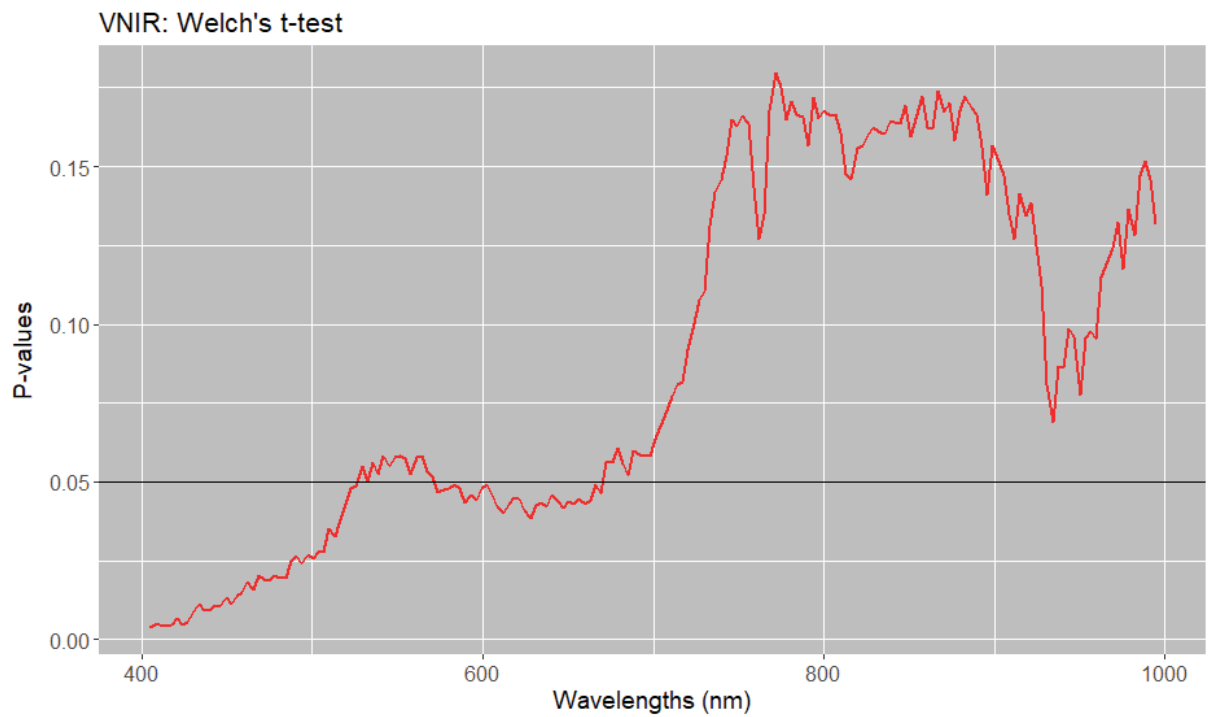
Figure 12: Plot of significant values from Welch's t-test across wavelengths from the VNIR sensor.

For the SWIR dataset, significant values (p-value < 0.05) were detected in the wavelength intervals between 1126-1137 nm, 1148-1153 nm, 1415-1426 nm and above 2448 nm (see figure 13).

Figure 13: Plot of significant values from Welch's t-test across wavelengths from the SWIR sensor.

In table 6 all the significant wavelengths from both sensors are collected which were used to fit prediction models.

Table 6: Significant wavelengths from Welch's t-test used to fit prediction models.

Dataset	Wavelengths (nm)
VNIR	405-526, 575-669
SWIR	1126-1137, 1148-1153, 1415-1426

Logistic regression models

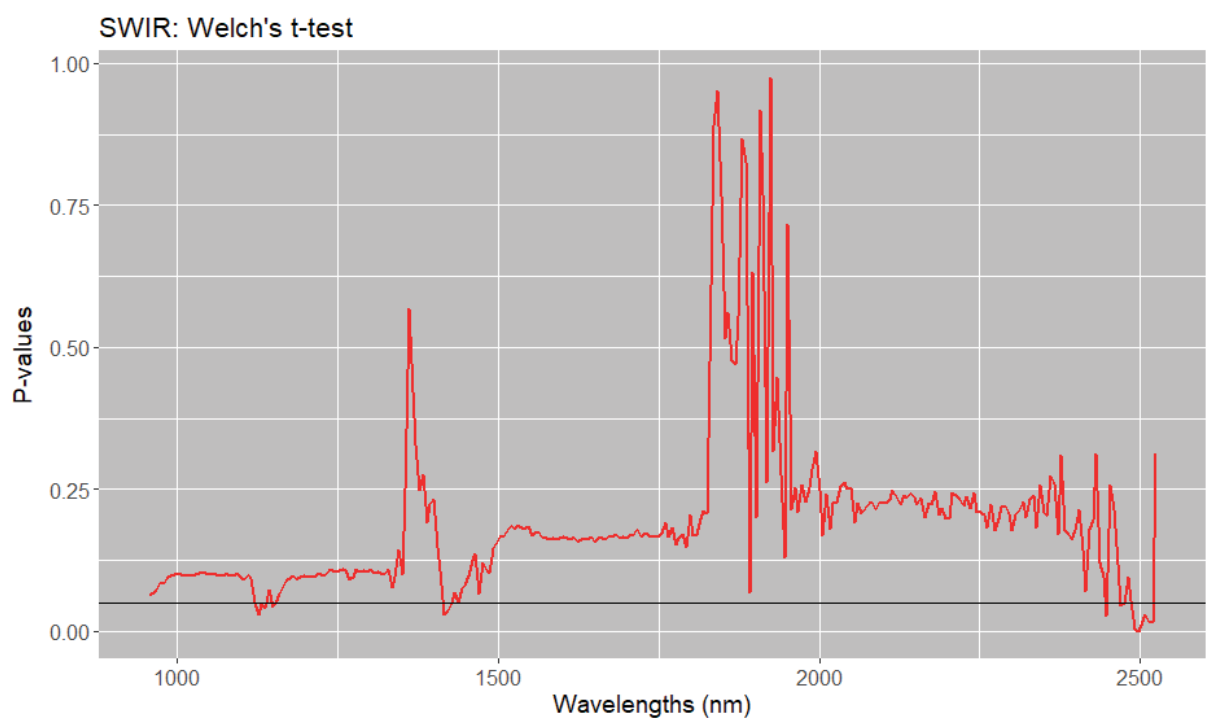For all and aggregated radiance values models, the mean prediction accuracy was 63 and 54%, Cohen's Kappa: 0.11 and 0.03 and area under the ROC curve: 0.61 and 0.54 respectively (see table 7). The best performing models had a mean prediction accuracy of 68 and 63%, Cohen's Kappa: 0.20 and 0.24 and area under the ROC curve: 0.69 and 0.57. The worst performing models had a prediction accuracy of 58 and 49%, Cohen's kappa: 0.10 and -0.05 and area under the ROC curve: 0.55 and 0.53.

Table 7: Performance of all logistic regression models.

Model nr.	Prediction accuracy		Cohen's kappa		ROC	
	All	Aggregated	All	Aggregated	All	Aggregated
1	0.66	0.63	0.16	0.24	0.67	0.57
2	0.61	0.53	0.07	0.03	0.57	0.47
3	0.66	0.55	0.12	0.08	0.59	0.50
4	0.61	0.59	0.08	0.13	0.57	0.59
5	0.68	0.53	0.20	0.00	0.69	0.58
6	0.58	0.49	0.10	-0.07	0.55	0.54
7	0.63	0.49	0.13	-0.05	0.65	0.50
8	0.65	0.55	0.15	0.08	0.62	0.54
9	0.60	0.49	0.07	-0.05	0.60	0.53
10	0.61	0.51	0.08	-0.08	0.57	0.53
Mean	0.63	0.54	0.11	0.03	0.61	0.54
SD	0.03	0.05	0.04	0.10	0.05	0.04

Overall, wavebands from both the VNIR and SWIR sensors were significant in logistic regression models (see figure 14). From the spectrum used to fit the models, several intervals

display a high count of significant wavebands. Waveband with wavelength 1131 nm was most frequent with 16 appearances followed by 602, 612 and 1126 nm with 14 appearances each.
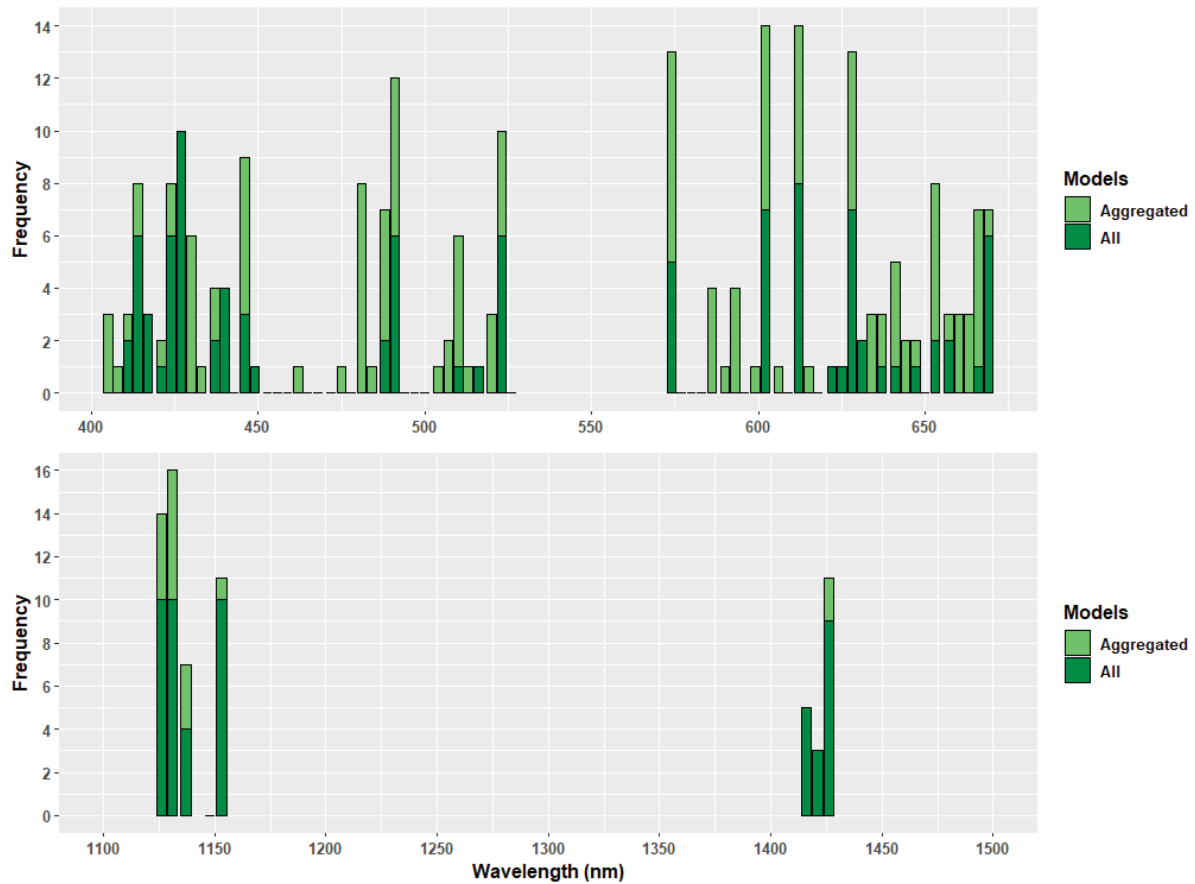
Figure 14: The 15 most significant wavebands in all logistic regression models. Dark green represents models fitted with all radiance values while light green represents models fitted with aggregated radiance values.

Random forest models

For all and aggregated radiance values models, the mean prediction accuracy was 63 and 62%, Cohen's kappa: 0.10 and 0.15 and area under the ROC curve: 0.55 and 0.57 respectively (see table 8). The best performing models had a prediction accuracy of 67%, Cohen's kappa: 0.17 and 0.31 and area under the ROC curve: 0.58 and 0.65. The worst performing models had a prediction accuracy of 57%, Cohen's kappa: 0.07 and -0.01 and area under the ROC curve: 0.53 and 0.49.

Table 8: Performance of all random forest models.

Model nr.	Prediction accuracy		Cohen's kappa		ROC	
	All	Aggregated	All	Aggregated	All	Aggregated
1	0.65	0.61	0.12	0.10	0.55	0.54
2	0.62	0.67	0.07	0.27	0.53	0.63
3	0.63	0.65	0.05	0.17	0.52	0.58
4	0.63	0.57	0.09	0.03	0.54	0.51
5	0.67	0.67	0.17	0.31	0.58	0.65
6	0.57	0.61	0.07	0.15	0.53	0.57
7	0.63	0.63	0.12	0.23	0.55	0.61
8	0.65	0.61	0.12	0.10	0.55	0.54
9	0.63	0.63	0.12	0.21	0.55	0.60
10	0.63	0.57	0.10	-0.01	0.54	0.49
Mean	0.63	0.62	0.10	0.15	0.55	0.57
SD	0.03	0.03	0.03	0.10	0.01	0.05

Mean decrease accuracy describes the significance of wavebands used in prediction. In this case how many individual pixels or trees are misclassified if the variable is removed from the model. In figure 15 the mean decrease prediction accuracy for wavebands used in the best model fitted to aggregated radiance values is plotted. As an example, the removal of waveband 1 with a wavelength of 404 nm from the aggregated model would cause misclassification of 9 trees.
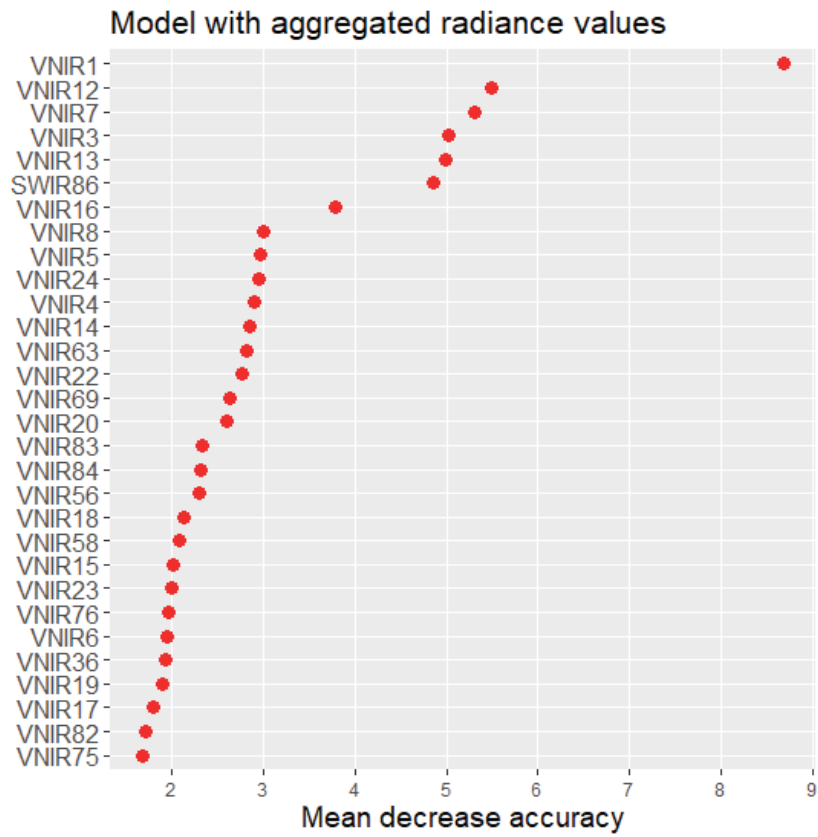
Figure 15: Mean decrease accuracy for wavebands used in the best random forest models fitted to aggregated radiance values.

Overall, wavebands from both the VNIR and SWIR sensor were significant (see figure 16). From the spectrum used to fit the models, wavelengths between 400-450 nm have the highest count of significant wavebands, but the wavelength intervals 1100-1150 nm and 1400-1425 nm also had a high frequency of significant wavebands. Few significant wavebands came from wavelengths between 550-650 nm. Waveband with wavelength 414 nm was most frequent with 18 appearances followed by 411 nm with 16 appearances.
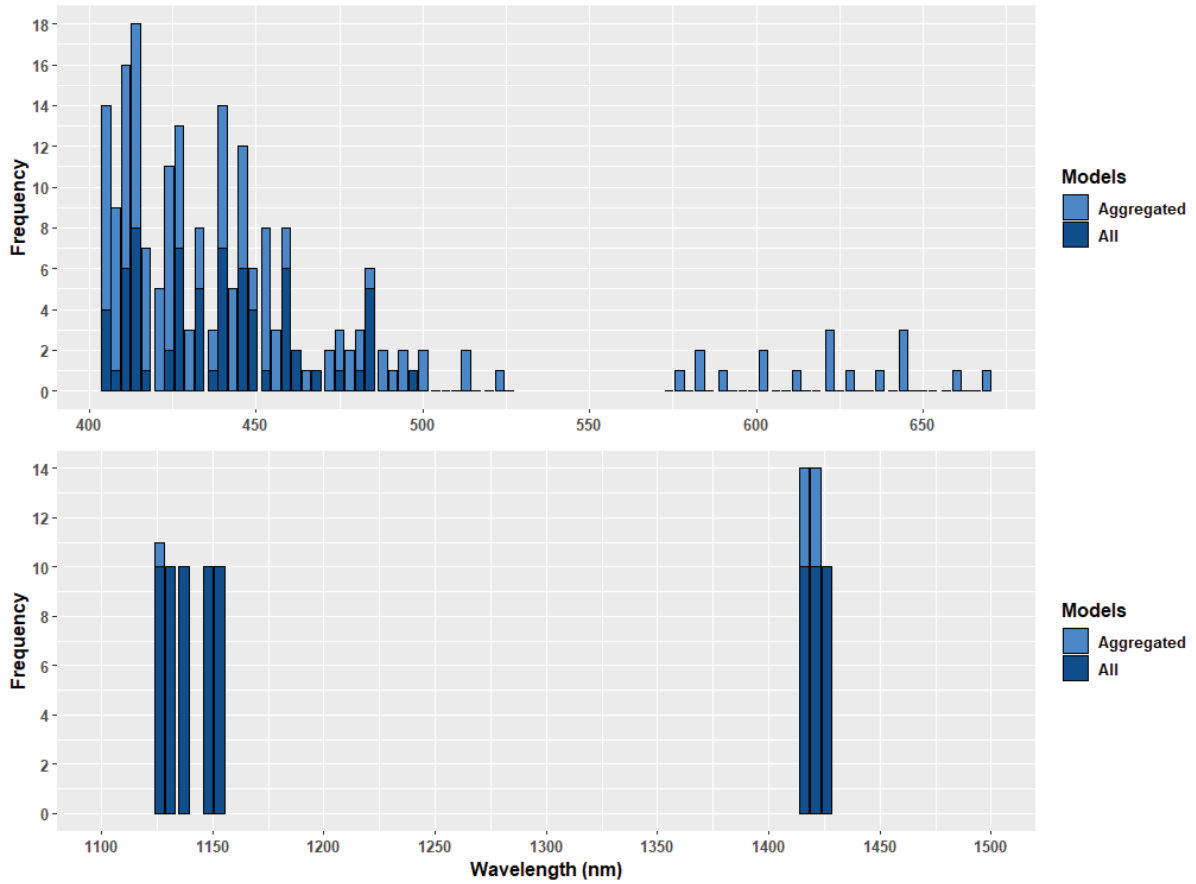
Figure 16: The 15 most significant wavebands in all random forest models. Dark blue represents models fitted with all radiance values while light blue represents models fitted with aggregated radiance values.

Compilation

For logistic regression and random forest models fitted to all radiance values mean prediction accuracy was 63%, Cohen's kappa: 0.11 and 0.10 and area under the ROC curve: 0.61 and 0.51 respectively (see table 9). For the models fitted to aggregated radiance values mean prediction accuracy was: 54 and 62%, Cohen's Kappa: 0.03 and 0.15 and area under the ROC curve: 0.54 and 0.57.

Table 9: Comparison of mean performance for logistic regression and random forest models.

Model and radiance value type	Prediction accuracy (mean/SD)	Cohen's kappa (mean/SD)	ROC (mean/SD)
Logistic regression (all)	0.63 / 0.03	0.11 / 0.04	0.61 / 0.05
Random forest (all)	0.63 / 0.03	0.10 / 0.03	0.55 / 0.01
Logistic regression (agg.)	0.54 / 0.05	0.03 / 0.10	0.54 / 0.04
Random forest (agg.)	0.62 / 0.03	0.15 / 0.10	0.57 / 0.05

Overall, wavebands from both the VNIR and SWIR sensors were significant (see figure 17). From the selected spectrum used to fit the models, wavelengths between 400-450 nm have the highest count of significant wavebands, but wavelengths between 1100-1150 nm and 1400-1425 nm also had a high frequency of significant wavebands. Wavebands with wavelengths 414 and 1131 nm were most frequent with 26 appearances each.
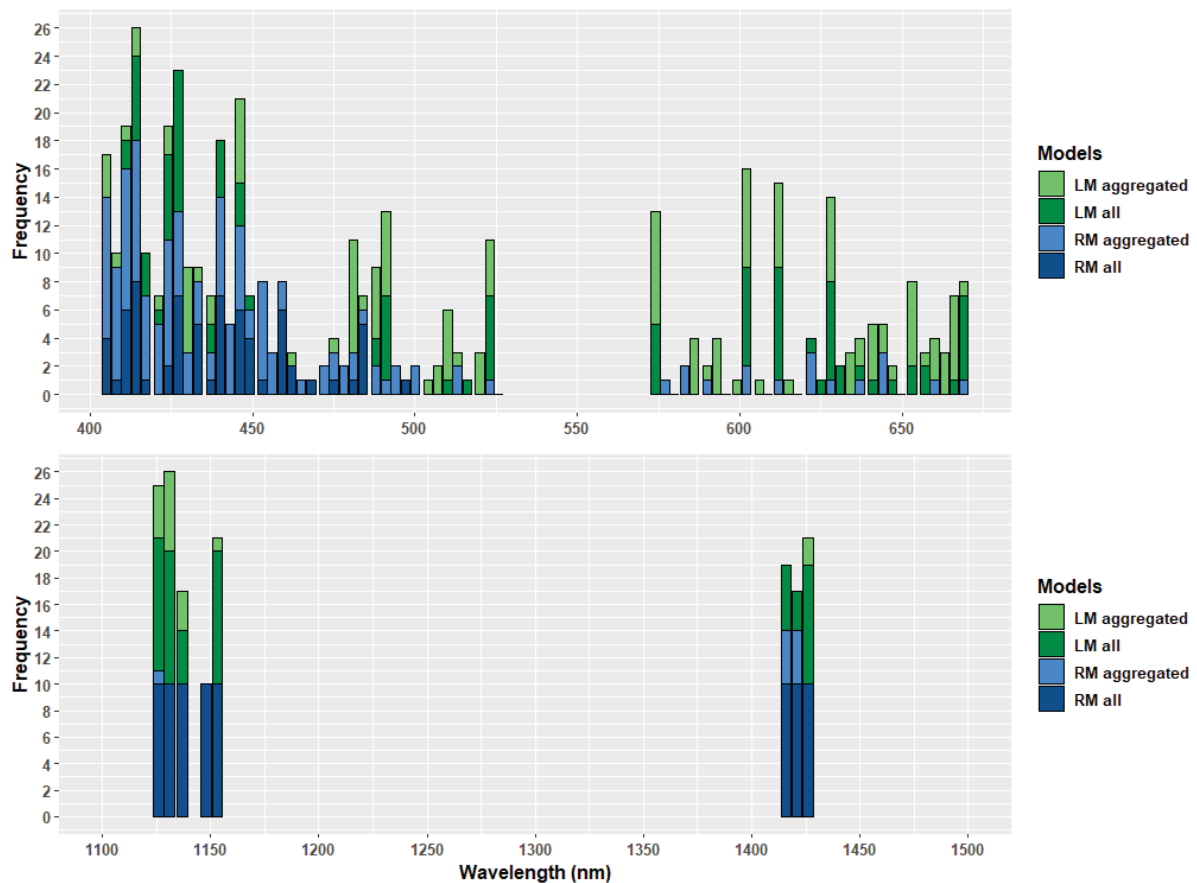
Figure 17: The 15 most significant wavebands in all models. Dark green represents logistic regression models fitted with all radiance values, light green represents logistic regression models fitted with aggregated values, dark blue represents random forest models fitted with all radiance values and light blue represents random forest models fitted with aggregated values.

Prediction map

The best random forest model fitted with aggregated radiance was used to create a prediction map over the study area (see figure 18). The prediction map is made up of ITCs, where each ITC is given a probability for rot between 0 and 1 based on the results from the prediction model. Data for the entire study area went through the same process as the data used for fitting

the models. All the pixels within ITC polygons contained an id that was used to extract the pixels. First, pixels with an NDVI value < 0.6 were removed, then the data was normalized and aggregated using normal mean. Lastly, the prediction model was used on the processed data and a prediction map was made.

Figure 18: Prediction of rot in ITCs from the study area.

Discussion

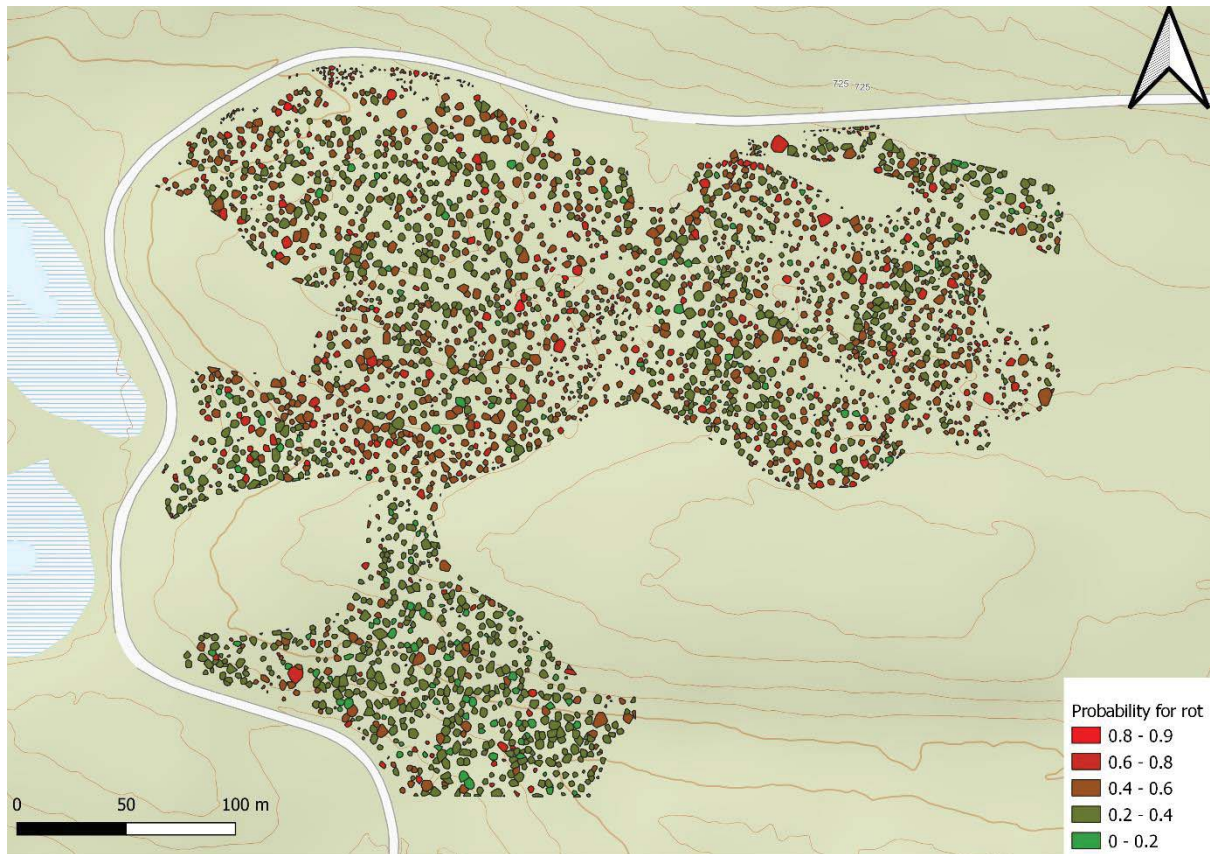All the infected stumps were classified after rot type during data collection. The classification of rot was later verified with senior research scientist at the NIBIO, Halvor Solheim. The review exposed errors in the data collection. Some of the classifications were wrong or impossible to classify based on the pictures taken. Visual inspection of rot requires expertise, and if the known symptoms for a syndrome are not found, it may be especially difficult to perform a correct classification. Additional, more thorough methods might be required (Schulze et al., 1997). During the review, it was concluded that DNA samples were necessary to classify rot 100% correctly. In this study, DNA sampling was not part of the field protocol due to budget constraints. This did not affect the outcome of the thesis, as the study seeks to examine if the combination of airborne hyperspectral images and laser scanning can be used to detect rot in spruce, not differentiate between rot types. It should also be noted that during the initial data collection performed by Moen (2020), wounds were observed in several trees along the edges of the study area that were in close approximation to the nearby road. The wounds were distributed over the entire length of the tree. During the construction of the nearby road, explosives were partially used. The probable cause for the wounds was determined to be caused by the previous road construction. Wounds can be the entrance for numerous fungi to establish themselves in spruce. Bleeding stereum (*Stereum sanguinolentum*) is a fungus known to infect wounds in spruce which is able to infect all types of wounds regardless of their age (Solheim, 2010). During the data collection, stumps were visually inspected for rot. This leaves the possibility of trees being classified as healthy even though the tree is infected. Rot could be present in higher parts of the tree that are not inspected. Still, the probability of many misclassifications caused by this is presumably low. Few trees in the dataset were in close approximation to the road. Additionally, Bleeding stereum is fairly uncommon. Solheim et al. (2017) inspected 1353 spruce stumps 20 years after selection felling and found Bleeding stereum in 3% of the stumps.

To extract the pixels from the hyperspectral images, they were matched with ITC polygons containing GNSS points registered during fieldwork. There are multiple algorithms used to detect single trees from which ITS polygons are created, and a different algorithm might have provided different results. Vauhkonen et al. (2011) compared different algorithms to detect single trees from ALS and concluded that forest structure strongly affected the performance of all algorithms. Some ITC polygons included several GNSS points and a Voronoi diagram was

implemented to split the ITC polygons into multiple trees. A weakness with this approach is the unnatural division of tree crowns where polygons contain multiple GNSS points as seen in figure 7. Parts of the divided polygon may belong to other trees within the same polygon. This is especially a problem to consider in cases were the polygon consists of both healthy and infected trees. Furthermore, some ITCs with a single GNSS point were made up of many pixels. It is possible that parts of the ITC belonged to other trees nearby, which were not part of the data collection. These trees could have a different classification. Sørhuus (2019) encountered the same problem in his extraction of hyperspectral pixels for statistical purposes. Only pixels that were positioned directly over GPS points were extracted in his study. The use of a buffer was considered to include more pixels around GNSS points. Sørhuus (2019) concluded that this method would risk the possibility of including pixels from neighboring trees or other objects and could benefit from accompanied laser data. For the current study, the use of ITCs in the extraction of pixels was an interesting approach which also enabled the ability to examine if the contribution of more pixels per tree resulted in better predictions relative to Sørhuus (2019).

The initial overview of the data revealed higher mean radiance values for healthy trees across multiple intervals of the analyzed spectrum in both the VNIR and SWIR datasets (see figures 10 and 11). Additionally, a substantial variation in the radiance values was observed. Partially, the difference between mean radiance value for healthy and infected trees was apparent, but the range in variance was also high in the same areas. Due to extensive variations, a common rule for distinguishing between healthy and infected trees was difficult to establish. Sørhuus (2019) experienced the same difficulties in his study with similar data from VNIR and SWIR sensors. Aside from high variations, the SWIR dataset faced additional challenges contributed by the combination of lower spatial resolution (i.e. less information) and noise. The SWIR dataset was resampled to match the spatial resolution of the image from the VNIR sensor, but the additional information obtained by using nearest neighbor resampling can affect the precision of the new image (Qianxiang et al., 2003). The effects of noise were apparent above 1800 nm in the SWIR dataset (see figure 11). In these wavelengths, there was little to no difference in mean radiance values or variation in both healthy and infected trees. This can also be seen in the wavelengths around 1400 nm, but the exploratory research did not reveal noise in this area. Multiple factors influence the radiance values registered from airborne hyperspectral images which can explain the noise. Aside from the sensor itself, and algorithms used to process the data, atmospheric state and solar zenith angle can affect the spectral quality

of the hyperspectral images (Kerekes & Hsu 2004). Große-Stoltenberg et al. (2016) explain that the distortion of registered radiance values from a SWIR sensor can be caused by light absorption from water vapor and high atmospheric gases. The sensor registers information in parts of the electromagnetic spectrum which are especially exposed to these phenomena. Weather data from the study area were not obtainable to substantiate this theoretical cause for noise in the dataset. The report from Terratec suggests that the data collection was affected by a limited weather window. Multiple attempts to collect data were performed, but only data from a successful attempt were kept and processed. Terratec were able to collect all the data during one flight which made this possible. Additionally, plants reflect less light in these parts of the electromagnetic spectrum, which can result in low or inadequate readings. Dalponte et al. (2013) and Sørhuus (2019) had similar radiance readings in several wavelength intervals from the SWIR sensor. By removing noise from the SWIR data, Dalponte et al. (2013) ended up discarding the data completely as the reduced data were insufficient for statistical purposes. Sørhuus (2019) also decided to exclude the SWIR data from his statistical modeling.

T-tests on aggregated radiance values showed significant differences between healthy and infected trees in several wavelengths for both the VNIR and SWIR datasets (see table 6). The difference could be explained by multiple factors and the presence of rot is one of them. Bendz-Hellgren and Stenlid (1995) and Bendz-Hellgren and Stenlid (1997) demonstrated that rot affects the growth and development of trees. Statistically significant wavelengths from the VNIR dataset were observed in the wavelength intervals 405-526 and 575-669 nm. This is similar to Sørhuus (2019) results where wavelengths between 415-485, 515-595 and > 700 nm were significant. This translates to the blue, green and near-infrared (NIR) parts of visible light in the electromagnetic spectrum. In this section of the electromagnetic spectrum, the color pigments of needles are visible. Changes in the color are directly affected by the needle's ability to perform photosynthesis. The process of photosynthesis is dependent on various inputs such as the availability of water and nutrients. The presence of root and butt rot can disturb a tree's ability to accumulate the inputs needed for photosynthesis thus altering the color of its needles (Solheim, 2010).

Regarding the SWIR dataset, statistically significant wavelengths were observed in the intervals 1126-1137, 1148-1153, 1415-1426 and above 2448 nm. This differs from Sørhuus (2019) who found significant p-values in all wavelengths except between wavelengths 1350-1450 nm. As previously mentioned, SWIR data can be affected by multiple factors resulting in

inadequate readings and should be closely examined to eliminate potential noise. Since the results from t-tests were used as selection criteria for wavebands to be included in the modeling, data from these wavebands were inspected further. The wavebands with significant wavelengths from 2448 nm and upwards included a lot of noise and were rejected during the exploratory research while the wavebands within wavelengths 1126-1137, 1148-1153 and 1415-1426 nm were kept. Sørhuus (2019) explained the lack of significant results around 1400 nm with the distortion from light absorption from water vapor. The differences in significant results could be explained by the atmospheric state at the time of data collection. Multiple studies involving hyperspectral data and the selection of wavebands indicate that direct comparisons of the selected wavebands are not possible (Dalponte et al., 2013; Leckie et al., 2004). Intricate variations in multiple factors can affect the information obtained from airborne hyperspectral images. The wavelengths in the SWIR dataset are from the infrared (IR) parts of the electromagnetic spectrum (Smith, 2000) which is known to reveal plant stress. Plant health can thereby be exposed from significant differences in these parts of the electromagnetic spectrum. Reduced health could be explained by a rot infection. However, abiotic factors such as water and soil conditions could also influence tree health. Previous studies show that soil properties can affect the development of butt rot in spruce. Mainly dry, sandy soils or soils with high pH facilitates infection and spreading of root and butt rot (Lindén & Vollbrecht, 2002). Geological data from the Geological survey of Norway (2015) showed that the bedrock in the study area was sandstone and the soil consisted of an incoherently, or thin cover, of moraine over the bedrock. Although sandy soil has shown to be a facilitator for root and butt rot, thin soil cover over bedrock can expose the forest to drought stress since water access is reduced. The soil cover is incoherently in the study area, enabling pockets of drought stressed trees to occur. Clark et al. (2005) found that radiance values were affected by the water level in the needles. If the water levels in some needles are a consequence of drought stress, this could undermine the effects of rot seen in radiance values. Visible drought stress was not observed during final felling or commented on by the forest owner, but an extensive summer drought occurred the year before the hyperspectral data acquisition and final felling.

Many factors can cause a disturbance in the radiance values recorded in hyperspectral images. The largest source of error in spectral imagery comes from variability in the illumination characteristics between the reference and target material (Analytik & Headwall Photonics Inc, 2016). Solar zenith angle and atmospheric state have already been mentioned, but a third source of illumination is often overlooked. Scattered light reflections from surrounding surfaces also

impact the illumination. The surrounding area and vegetation alongside with variations in the canopy cover may alter the radiance values registered in a pixel. Aiazzi et al. (2006) and Rasti et al. (2018) described these factors in their studies. Hence, the geographical position can cause distortion. The position of the forest relative to the surrounding area, inclination and inclination angle affects the solar irradiance and scattered light reflections (Lowe et al., 2017).

The performance of logistic regression models for all radiance values was overall better compared to the ones for aggregated radiance values (see table 7). Models fitted to all radiance values had a mean prediction accuracy of 63% ranging from 58-68%. For models fitted to aggregated values the mean prediction accuracy was 54% and ranged from 49-63%. Cohen's kappa (0.11 vs. 0.03) and area under the ROC curve (0.61 vs. 0.54) were also higher for models fitted to all radiance values indicating that these models had better reliability between observed and predicted classes and had a higher degree of correct classifications. The most significant wavebands included in the models showed some differences in which wavelengths were the most important predictors (see figure 14). Models fitted to all radiance values tended to favor wavebands from the SWIR sensor and the lower spectrum of the VNIR sensor between wavelengths 400-450 nm. Models fitted to aggregated radiance values included some wavebands from the SWIR sensor, but most were from the VNIR sensor in wavelengths 475-525 and 575-650 nm. Significant wavebands appear to come from all parts of the included spectrum, but some wavebands stand out. None of the significant wavebands were included in all models, but wavebands with wavelengths: 427, 491, 523, 574, 602, 612, 629, 1126, 1131, 1153 and 4269 nm were present in 50% or more of the models.

The performance of random forest models for all radiance values was similar in comparison to the ones for aggregated radiance values (see table 8). Mean prediction accuracy was 63 and 62% and ranged from 57-67%. All models had low variance in the model validations used to measure their performance. Models fitted to aggregated radiance values outperformed the models fitted to all radiance values in all model evaluations except mean prediction accuracy with Cohen's kappa (0.15 vs. 0.10) and area under the ROC curve (0.57 vs. 0.55) respectively. Examining the most significant wavebands (see figure 16), there is an apparent contrast in which wavelengths the models have incorporated. Models fitted to all radiance values have the most significant wavebands from the SWIR sensor between wavelengths 1100-1150, 1400-1450 nm and in the wavelengths 400-500 nm from the VNIR sensor. No wavebands in wavelengths between 500-675 nm were significant. The models fitted to aggregated radiance

values had few significant wavebands from the SWIR sensor compared to the VNIR sensor. Most of the significant wavebands were from the wavelengths 400-500 nm, but the models also included significant wavebands in wavelengths 500-675 nm. Significant wavebands appear to come from all parts of the included spectrum, but few come from wavelengths between 500-675 nm. None of the significant wavebands were included in all models, but all wavebands from the SWIR sensor were present in 50% or more of the models. For the VNIR sensor, this was the case for wavelengths: 405, 411, 414, 424, 427, 440 and 446 nm.

It is interesting to further compare the mean performance of the logistic regression and random forest models (see table 9). The performance was better when both were fitted to all radiance values and there where little discrepancy in performance between the two methods. Mean prediction accuracy was the same: 63%, but the overall variance in performance was lower for the random forest models. The logistic regression models had higher mean Cohen's kappa: 0.11 vs. 0.10, and area under the ROC curve: 0.61 vs. 0.55. The low mean Cohen's kappa for the random forest models indicates that the relation between illegitimate and legitimate classifications was close to 1, meaning the models predicted almost the same amount of correct and wrong classifications. The performance of the forest regression models was more similar with almost the same mean prediction accuracy: 63 and 62%. The difference was larger in Cohen's kappa: 0.10 and 0.15, and area under the ROC curve: 0.55 and 0.57. There was a greater span in the logistic regression models performance. The disparity in prediction accuracy: 63 and 54%, was quite high with almost a 10% difference. Cohen's kappa: 0.11 and 0.03, and area under the ROC curve: 0.61 and 0.54, was also considerably different which suggests the logistic regression models made better predictions when they were fitted to larger datasets. The results are slightly better compared to Sørhuus (2019). When he fitted models to all his data, he got a prediction accuracy of 55 and 59% for his logistic regression and random forest models. Cohan's kappa: 0.11 vs. 0.00 and area under the ROC curve: 0.61 vs. 0.51 were also higher for the logistic regression models in this study. Comparing the random forest models, Cohen's kappa: 0.10 and area under the ROC curve: 0.55 were the same in both studies.

The most significant wavebands (see figure 17) for all models were also compared, and some trends are visible. Wavebands from the SWIR sensor showed a high degree of significance with multiple appearing in over 50% of the models. There is also a clear distinction between wavebands in wavelengths 400-525 and 575-675 nm. The latter has some singular wavebands

which appeared in many models, but these are constricted to logistic regression models and few wavebands from random forest models were present in this spectral interval. The former is more balanced with multiple wavebands appearing in both logistic regression and random forest models. Furthermore, wavebands in wavelengths between 400-525 nm accounted for 70% of all significant wavebands from the VNIR sensor. Wavebands with wavelengths: 414, 427, 446, 1126, 1131, 1153 and 1426 nm were present in 50% or more of the models indicating that the lower end of the visible spectrum and infrared were most significant for prediction models in this study. Sørhuus (2019) found contradicting results with most significant wavelengths in higher parts of the visible spectrum and near-infrared: 705, 762, 833, 899 and 944 nm. This underlines the problem of direct comparisons of significant wavelengths as troublesome.

The difference in significant wavebands for logistic regression and random forest models illustrates the different approaches the models incorporate in their fittings and the influence of size for training datasets. The results indicate that logistic regression and random forest models are sensitive to the size and information in the data they are fitted to. When small, the quality of the data becomes crucial for the performance of the model and this has a large impact on significant wavebands. Larger sample size could have contributed to less difference in performance and highlighted the significant wavebands more clearly. In this study, the logistic regression models were more sensitive and gave better predictions when fitted to larger datasets. Overall, the logistic regression models gave better predictions. The results contradict what Sørhuus (2019) found in his study. He found that the random forest models performed better than the logistic regression models. This can probably be explained by how the logistic regression and random forest model are fitted to their training datasets. A closer look at the individual models reveals intriguing results (see table 7 and 8). Three out of the four best performing models were fitted to the same dataset. This was also the case for the worst-performing models, indicating that the performance is depended on the random sample the models are fitted to. The range in prediction accuracy, 57-68%, is comparable to Sørhuus (2019) which got a prediction accuracy ranging from 51-71% in his models. The mean prediction accuracy was higher in this study for both logistic regression models 63 vs. 55% and random forest models 63 vs. 59%. It is unclear how many times the models in Sørhuus (2019) study were fitted. For this study logistic regression and random forest models were fitted 10 times: once per random sample used for training. How many times the models are fitted can affect prediction accuracy. This applies to both range and mean. This is especially the case for

random forest models that uses bootstrap. Numerous fittings to the same training dataset could lead to different results. The random forest model builds multiple decision trees from random samples within the same training dataset. This presents the possibility of a wider range in performance for models fitted to the same training dataset dependent on the bootstrapping performed at each fitting. The random forest models were fitted once per training dataset. If the random forest model were fitted several times, this could have led to overall better performance and may have outperformed the logistic regression models. The absence of multiple fittings is due to a lack of capacity.

When deciding between which sensor is most beneficial for detecting rot, the VNIR sensor seems to be the better option with more significant wavebands, and less noise, present in its data compared to the data from the SWIR sensor. This coincides with Dalponte et al. (2013) experience. He found data in wavelengths above 1500 nm from the SWIR sensor to be inconclusive. Classifications in this part of the electromagnetic spectrum become challenging as the plants begin to reflect less light (Große-Stoltenberg et al., 2016). The exploratory research and t-tests did, however, show several significant wavelengths without noise between 1100-1400 nm in the SWIR data. The infrared spectrum can expose plant stress, and wavelengths 1126, 1131, 1153 and 1426 nm were present and significant in 50% or more of the models. Although SWIR data can be troublesome in classification, this study shows potential in the infrared spectrum. The SWIR sensor should not be ruled out as an option but considered an addition to the VNIR sensor in rot prediction. The models in this study were not fitted without data from the SWIR, so the benefits of the additional information provided is uncertain.

The aid of ALS did increase the performance of the models compared to Sørhuus (2019), but not significantly. The models still give unreliable results in detecting rot with a mean prediction accuracy of 63%. A higher number of observations and multiple fittings of the random forest models could have resulted in better models for this study. Furthermore, the method used to designate pixels to different trees using ITC polygons needs to be improved. The unnatural division of ITCs polygons containing both healthy and infected trees probably caused some pixels to be classified incorrectly. This could cause an imbalance in the data, making it difficult for the models to discriminate between significant wavelengths. The combination of airborne hyperspectral images and laser scanning also presents other challenges. The combination enables the collection of large quantities of data which burdens data processing. The process

of filtering out significant wavelengths in the electromagnetic spectrum affected by rot becomes complicated, and the possibility of excluding relevant data presents itself. The difference in significant wavelengths between Sørhuus (2019) study and this study substantiates this theory. Likewise, data collection from airborne hyperspectral images in different studies have proven to give various significant wavelengths (Leckie et al., 2004).

If further improvements prove the method viable, it might be possible to predict the occurrence of rot in spruce with high accuracy using a combination of airborne hyperspectral images and laser scanning. The constant development and improvement of hyperspectral sensors could also assist the development of prediction models. It remains to be seen if the benefits outweigh the costs. Assuming such models can be developed, they can be used to produce prediction maps. The spreading dynamics of root and butt rot makes the infected trees mostly appear in clusters. These maps could potentially reveal the distribution of root and butt rot in a forest, and where they are concentrated. This could contribute to advances in forest management and gives the forest owners a tool to reduce the economic loss caused by root and butt rot. Areas with a high concentration of infected trees could be prioritized in felling to reduce the loss. Furthermore, troublesome areas could be altered by planting a different tree species during regeneration that is not receptive to the present fungi. Thus, contribute to maximizing the utilization of available forest resources.

Conclusion

The goal of this study was to explore if the combination of airborne hyperspectral images and laser scanning can be used to identify root and butt rot in Norway spruce with high accuracy. The results indicate that there is a significant difference in the radiance value between healthy and infected trees, but it is difficult to determine a defined rule to separate them from each other. Multiple factors could have contributed to this problem. The dataset was relatively small. Pixels classified incorrectly because of the method applied in fieldwork and implementation of ITC. Variations in the registered radiance values for each wavelength which differed largely from the mean radiance value were observed. Welch's t-test found several significant wavelengths, but there was little cohesion in the models. Impacts from solar zenith angle, atmospheric state, landscape and drought stress can cause additional distortion in radiance values both directly and indirectly.

Logistic regression and random forest models were fitted to data from a hyperspectral image to predict the occurrence of root and butt rot in spruce. The performance for both was the same, with a mean prediction accuracy of 63%. The inclusion of ALS did improve the model slightly compared to previous studies. The method leaves room for improvement, but there is potential in combining airborne hyperspectral images and laser scanning to detect root and butt rot in Norway spruce with high accuracy. If the number of observations is increased, and the implementation of ITC is improved, this could result in models with satisfactory prediction accuracy.

References

Adão, T., Hruška, J., Pádua, L., Bessa, J., Peres, E., Morais, R. & Sousa, J. J. (2017). Hyperspectral Imaging: A Review on UAV-Based Sensors, Data Processing and Applications for Agriculture and Forestry. *Remote Sensing*, 9 (11). doi: 10.3390/rs9111110.

Aiazzi, B., Alparone, L., Barducci, A., Baronti, S., Marcoionni, P., Pippi, I. & Selva, M. (2006). Noise modelling and estimation of hyperspectral data from airborne imaging spectrometers. *Annals of Geophysics*, 49 (1). doi: 10.4401/ag-3141.

Analytik & Headwall Photonics Inc. (2016). *Airborne Hyperspectral and Ground-Truth Technologies*. Available at: http://www.analytik.co.uk/wp-content/uploads/2016/03/airborne-hyperspectral-and-ground-truth-technologies.pdf (accessed: 20.05.2020).

Anderson, J. E., Plourde, L. C., Martin, M. E., Braswell, B. H., Smith, M. L., Dubayah, R. O., Hofton, M. A. & Blair, J. B. (2008). Integrating waveform lidar with hyperspectral imagery for inventory of a northern temperate forest. *Remote Sensing of Environment*, 112 (4): 1856-1870. doi: 10.1016/j.rse.2007.09.009.

Bendz-Hellgren, M. & Stenlid, J. (1995). Long-term reduction in the diameter growth of butt rot affected Norway spruce, *Picea abies*. *Forest Ecology and Management*, 74 (1-3): 239-243. doi: 10.1016/0378-1127(95)03530-N.

Bendz-Hellgren, M. & Stenlid, J. (1997). Decreased volum growth of *Picea abies* in response to *Heterobasidon annosum* infection. *Canadian Journal of Forest reaserch*, 27 (10): 1519-1524. doi: 10.1139/x97-104.

Bjørbæk, L. H. (2016). *Råte i høyereliggende granskog på Østlandet*. Master's thesis. Ås: Norwegian University of Life Sciences. Available at: http://hdl.handle.net/11250/2403128 (accessed: 17.03.2020).

Bollandsås, O. M., Ørka, H. O., Dalponte, M., Gobakken, T. & Næsset, E. (2019). Modelling Site Index in Forest Stands Using Airborne Hyperspectral Imagery and Bi-Temporal Laser Scanner Data. *Remote Sensing*, 11 (9). doi: 10.3390/rs11091020.

Breidenbach, J., Bøhn, N., Dalen, L. S., Eriksen, R., Fjellstad, K. B., Gjerde, I., Granhus, A., Gundersen, V., Hindrum, R., Holt- Hanssen, K., et al. (2018). *Bærekraftig skogbruk i Norge*. Available at: http://www.skogbruk.nibio.no/skogen-i-norge-1/ (accessed: 20.04.20).

Cao, F., Yang, F., Ren, J., Jiang, J. & Ling, W.-K. (2017). *Does Normalization Methods Play a Role for Hyperspectral Image Classification?* ArXiv. Available at: https://arxiv.org/ftp/arxiv/papers/1710/1710.02939.pdf.

Carson, G., Manic, I., Pisarenco, M., Li, L., Reutersward, P. & Sandsten, M. (2006). *Detection of tree rot in living trees*. Eindhoven university of technology. p. 13.

Chrzanowski, M. (2014). Weighted empirical likelihood inference for the area under the ROC curve. *Journal of Statistical Planning and Inference*, 147: 159-172. doi: 10.1016/j.jspi.2013.11.011.

Clark, M. L., Roberts, D. A. & Clark, D. B. (2005). Hyperspectral discrimination of tropical rain forest tree species at leaf to crown scales. *Remote Sensing of Environment*, 96 (3-4): 375-398. doi: 10.1016/j.rse.2005.03.009.

Dalen, L. S. (2018). *Ny kunnskap skal redde skogen fra råte*. Available at: https://www.nibio.no/nyheter/ny-kunnskap-skal-redde-skog-fra-rate (accessed: 16.04.2020).

Dalponte, M., Ørka, H. O., Gobakken, T., Gianelle, D. & Næsset, E. (2013). Tree Species Classification in Boreal Forests With Hyperspectral Data. *IEEE Transactions on Geoscience and Remote Sensing*, 51 (5): 2632-2645. doi: 10.1109/TGRS.2012.2216272.

Dalponte, M., Ørka, H. O., Ene, L. T., Gobakken, T. & Næsset, E. (2014). Tree crown delineation and tree species classification in boreal forests using hyperspectral and ALS data. *Remote Sensing of Environment*, 140: 306-317. doi: 10.1016/j.rse.2013.09.006.

Dalponte, M. (2018). *itcSegment: Individual Tree Crowns Segmentation* (Version 0.8). R package. Available at: https://CRAN.R-project.org/package=itcSegment.

Eid, T., Gobakken, T. & Næsset, E. (2004). Comparing stand inventories for large areas based on photo-interpretation and laser scanning by means of cost-plus-loss analyses. *Scandinavian Journal of Forest Research*, 19 (6): 512-523. doi: 10.1080/02827580410019463.

Fjærli, A. F. (2016). *Råte i gran på Nord-Vestlandet*. Master's thesis. Ås: Norwegian University of Life Sciences. Available at: http://hdl.handle.net/11250/2403126 (accessed: 16.03.2020).

Geological survey of Norway. (2015). *National bedrock database for bedrock*. Available at: http://geo.ngu.no/kart/berggrunn/?lang=English (accessed: 18.05.20).

Grahn, H. & Geladi, P. (2007). *Techniques and Applications of Hyperspectral Image Analysis*. 1st ed. Hoboken, New Jersey: Wiley.

Granhus, A. & Hylen, G. (2016). *Prosjektet «Råte i granskog – utbredelse og konsekvenser for valg av omløpstid». Sluttrapport*. NIBIO Rapport vol. 2 nr. 40. Available at: http://hdl.handle.net/11250/2380089 (accessed: 16.03.2020).

Greig, B. J. W. (1998). Field recognition and diagnosis of Heterobasidion annosum. In *Heterobasidion annosum: Biology, Ecology, Impact and Control*, pp. 35-42. Oxford: CAB International.

Große-Stoltenberg, A., Hellmann, C., Werner, C., Oldeland, J. & Thiele, J. (2016). Evaluation of Continuous VNIR-SWIR Spectra *versus* Narrowband Hyperspectral Indices to Discriminate the Invasive *Acacia longifolia* within a Mediterranean Dune Ecosystem. *Remote Sensing*, 8 (4). doi: 10.3390/rs8040334

Hanssen, K. H., Solberg, S., Hietala, A. M., Krokene, P., Rolstad, J., Solheim, H. & Økland, B. (2019). *Skogskader - en kunnskapssammenstilling*. NIBIO Rapport vol. 5 nr. 143. Available at: http://hdl.handle.net/11250/2632291 (accessed: 15.03.2020).

Huse, K. J. (1983). *Forekomst av råte i norsk granskog*. Rapport fra Norsk Institutt for Skogforskning 03/1983: 1-39.

Huse, K. J., Venn, K. & Solheim, H. (1994). *Stump inventory of root and butt rots in Norway spruce cut in 1992*. Rapport fra skogforskningen 23/1994. Available at: http://hdl.handle.net/11250/2560332 (accessed: 15.03.2020).

HySpex. (n.d.). *HySpex Classic*. Available at: https://www.hyspex.com/hyspex-products/hyspex-classic/ (accessed: 01.02.2020).

Ju, Y., Pan, J., Wang, X. & Zhang, H. (2014). Detection of *Bursaphelenchus xylophilus* infection in *Pinus massoniana* from hyperspectral data. *Nematology*, 16 (10): 1197-1207. doi: 10.1163/15685411-00002846.

Kandare, K. (2017). *Fusion of airborne laser scanning and hyperspectral data for predicting forest characteristics at differernt spatial scales*. Doctoral thesis. Ås: Norwegian University of Life Sciences. Available at: https://static02.nmbu.no/mina/forskning/drgrader/2017-Kandare.pdf (accessed: 24.03.2020).

Kandare, K., Ørka, H. O., Dalponte, M., Næsset, E. & Gobakken, T. (2017). Individual tree crown approach for predicting site index in boreal forests using airborne laser scanning and hyperspectral data. *International Journal of Applied Earth Observations and Geoinformation*, 60: 72-82. doi: 10.1016/j.jag.2017.04.008.

Kangas, A., Gobakken, T., Puliti, S., Hauglin, M. & Næsset, E. (2018). Value of airborne laser scanning and digital aerial photogrammetry data in forest decision making. *Silva Fennica*, 52 (1). doi: 10.14214/sf.9923.

Kerekes, J. P. & Hsu , S. M. (2004). Spectral Quality Metrics for VNIR and SWIR Hyperspectral Imagery. *Conference Proceedings of SPIE*, 5425. doi: 10.1117/12.542192.

Korhonen, K. & Stenlid, J. (1998). Biology of *Heterobasidion annosum*. In *Heterobasidion annosum : Biology, Ecology, Impact and Control*, pp. 43-70. Oxford: CAB International.

Larsson, B., Bengtsson, B. & Gustafsson, M. (2004). Nondestructive detection of decay in living trees. *Tree Physiology*, 24 (7): 853-858. doi: 10.1093/treephys/24.7.853.

Leckie, D. G., Jay, C., Gougeon, F. A., Sturrock, R. N. & Paradine, D. (2004). Detection and assessment of trees with *Phellinus weirii* (laminated root rot) using high resolution multi-spectral imagery. *International Journal of Remote Sensing*, 25 (4): 793-818. doi: 10.1080/0143116031000139926.

Leica Geosystems AG. (n.d.). *Leica ALS70 - Arborne Laser Scanners Performance for diverse Applications*. Available at: http://w3.leica-geosystems.com/downloads123/zz/airborne/ALS70/brochures/Leica_ALS70_6P_BRO_en.pdf (accessed: 01.04.2020).

Liaw, A. & Wiener, M. (2002). *Classification and Regression by randomForest* (Version 4.6.14). R package. Available at: https://cran.r-project.org/web/packages/randomForest/index.html (accessed: 20.05.20).

Lillesand, T. M., Kiefer, R. W. & Chipman, J. W. (2008). *Remote Sensing and Image Interpretation*. 6th ed. Madison, Wisconsin: Wiley.

Lindén, M. & Vollbrecht, G. (2002). Sensitivity of Picea abies to Butt Rot in Pure Stands and in Mixed Stands with Pinus sylvestris in Southern Sweden. *Silva Fennica*, 36 (4): 767-778. doi: 10.14214/sf.519.

Lowe, A., Harrison, N. & French, A. P. (2017). Hyperspectral image analysis techniques for the detection and classification of the early onset of plant disease and stress. *Plant methods*, 13 (80). doi: 10.1186/s13007-017-0233-z.

Maltamo, M., Næsset, E. & Vauhkonen, J. (2014). *Forestry Applications of Airborne Laser Scanning : Concepts and Case Studies*. 1st ed. Dordrecht: Springer.

McHugh, M. L. (2012). Interrater reliability: the kappa statistic. *Biochemia Medica*, 22 (3): 276-282. doi: 10.11613/BM.2012.031.

Ministry of Agriculture and Food. (2015). *SKOG22*. Nasjonal strategi for skog- og
    trenæringen. Available at:
    https://www.regjeringen.no/contentassets/711e4ed8c10b4f38a699c7e6fdae5f43/skog_
    22_rapport_260115.pdf (accessed: 03.04.2020).

Ministry of Agriculture and Food. (2018). *Forestry*. Available at:
    https://www.regjeringen.no/en/topics/food-fisheries-and-
    agriculture/skogbruk/innsikt/skogbruk/id2009516/ (accessed: 16.04.2020).

Moen, O. M. (2020). *Predicting the extent of root and butt rot in stems of Norway spruce
    (Picea abies)*. Master's thesis in submission. Ås: Norwegian University of Life
    Sciences.

Molin, N. (1957). Om *Fommes annosus* spridningsbiologi. *Meddelanden från Statens
    skogsforskningsinstitut*, 47 (3): 36.

Moorthy, I., Miller, J. R. & Noland, T. L. (2008). Estimating chlorophyll concentration in
    conifer needles with hyperspectral data: An assessment at the needle and canopy
    level. *Remote Sensing of Environment*, 112 (6): 2824-2838. doi:
    10.1016/j.rse.2008.01.013.

Næsvold, B. H. (1989). *Forekomst av råte i eldre granskog : en undersøkelse under hogst og
    på hogstflatene i Nord-Trøndelag*. NTF-rapport 01/1989. Steinkjer.

NASA Earth Observatory. (2000). *Normalized Diffrence Vegetation Index (NDVI)*. Available
    at:
    https://earthobservatory.nasa.gov/features/MeasuringVegetation/measuring_vegetatio
    n_2.php (accessed: 03.05.2020).

Norsk Elektro Optikk AS. (n.d.). *Norsk Elektro Optikk As - A leading photonics company*.
    Available at: http://neo.no/home (accessed: 01.03.2020).

Norsk Virkesmåling. (2015a). *Målereglement Massevirke*. Available at:
    http://www.m3n.no/wp-content/uploads/2017/09/B2_Maalereglement_massevirke.pdf
    (accessed: 13.04.2020).

Norsk Virkesmåling. (2015b). *Målereglement Sagtømmer*. Available at:
    http://www.m3n.no/wp-content/uploads/2017/09/B1_Maalereglement_sagtommer.pdf
    (accessed: 13.04.2020).

Norsk Virkesmåling. (2018). *Vedtekter for Norsk Virkesmåling*. Available at:
    www.m3n.no/om-oss/vedtekter/ (accessed: 16.04.20).

Norwegian Agriculture Agency. (2020). *Tømmeravirkning og - priser*. Available at: https://www.landbruksdirektoratet.no/no/statistikk/skogbruk/tommeravvirkning (accessed: 13.04.2020).

Norwegian Mapping Authority. (2017). *Positioning*. Available at: https://www.kartverket.no/en/Positioning/ (accessed: 20.05.20).

QGIS Geographic Information System. (2020). *Open Source Geospatial Foundation Project* (Version 3.10.3). Software: QGIS Development Team. Available at: http://qgis.osgeo.org (accessed: 01.04.20).

Qianxiang, Z., Zhongliang, J. & Shizhong, J. (2003). *Remote sensing image fusion for different spectral and spatial resolutions with bilinear resampling wavelet transform*. Proceedings of the 2003 IEEE International Conference on Intelligent Transportation Systems, Shanghai, China.

R Core Team. (2020). *R: A language and environment for statistical computing* (Version 4.0.0). Programming language: R Foundation for Statistical Computing. Available at: https://www.R-project.org/ (accessed: 01.04.20).

Rasti, B., Scheunders, P., Ghamisi, P., Licciardi, G. & Chanussot, J. (2018). Noise reduction in hyperspectral Imagry: Overview and application. *Remote Sensing*, 3 (3). doi: 10.3390/rs10030482.

Redfern, D. B. & Stenlid, J. (1998a). Spore dispersal and infection. In *Heterobasidion annosum: Biology, Ecology, Impact and Control*, pp. 105-124. Oxford: CAB International.

Redfern, D. B. & Stenlid, J. (1998b). Spread within the tree and stand. In *Heterobasidion annosum: Biology, Ecology, Impact and Control*, pp. 125- 141. Oxford: CAB International.

ReSe. (n.d.). *PARGE Image Rectification*. Available at: https://www.rese-apps.com/software/parge/index.html (accessed: 16.04.20).

Schulze, S., Bahnweg, G., Tesche, M. & Sandermann, J. H. (1997). Identification techniques for *Armillaria spp*. and *Heterobasidion annosum* root and butt rot diseases. *Archives of Phytopathology & Plant Protection*, 31 (2): 141-163. doi: 10.1080/03235409709383225.

Skogbrukslova. (2005). *Lov om skogbruk av 27. mai 2005 nr. 31*. Available at: https://lovdata.no/dokument/NL/lov/2005-05-27-31 (accessed: 20.05.20).

Smith, W. J. (2000). *Modern Optical Engineering: The Design of Optical Systems*. 3rd ed. New York: McGraw-Hill.

Solheim, H. & Holen, C. O. (1990). Rotråte - et sunnhetsproblem i norsk granskog. *Norsk skogbruk*, 36 (5): 26-27.

Solheim, H. (2006). *White rot fungi in living Norway spruce trees at high elevation in southern Norway with notes on gross characteristics of the rot*. Aktuelt fra skogforskningen 01/2006: 5-12. Available at: http://hdl.handle.net/11250/2557600 (accessed: 21.03.2020).

Solheim, H. (2010). *Råtesopper - i levende trær*. Brochure: Norwegian Forest and Landscape Institute. Available at: http://hdl.handle.net/11250/2469366 (accessed: 14.03.2020).

Solheim, H., Fossdal, C. G. & Hietala, A. M. (2012). Klimavinnerne. Rotkjuke–granas verste fiende. *Norsk skogbruk* (4): 74.

Solheim, H., Granhus, A. & Scholten, J. (2017). *Råte i granbestand 20 år etter selektiv hogst*. NIBIO Sluttrapport. Available at: http://www.skogtiltaksfondet.no/userfiles/files/Prosjektrapporter/2017/2015-40_R%C3%A5te%20i%20granbestand%2020%20%C3%A5r%20etter%20selektiv%20hogst.pdf (accessed: 16.04.2020).

Solli, P.-G., Arnekleiv, G., Bergsaker, E., Nordby, H., Rødland, K. A., Stuve, I. & Nilsen, J.-E. Ø. (2013). *Skogbruksplanlegging - Formål, behov og organisering*. Statens landbruksforvaltning rapport 05/2013. Available at: http://gammel.kystskogbruket.no/userfiles/files/Rapport.pdf (accessed: 23.03.2020).

Sørhuus, Ø. (2019). *Bruk av flybåren hyperspektralsensor for påvisning av råte istående granskog (Picea abies)*. Master's thesis. Ås: Norwegian University of Life Sciences. Available at: http://hdl.handle.net/11250/2601373 (accessed: 01.01.2020).

Statistisk Sentralbyrå. (2018). *The National Forest Inventory, 30. August 2019*. Available at: https://www.ssb.no/en/jord-skog-jakt-og-fiskeri/statistikker/lst (accessed: 01.03.2020).

Statistisk Sentralbyrå. (2020). *Rekordhøy tømmerhogst*. Available at: https://www.ssb.no/jord-skog-jakt-og-fiskeri/artikler-og-publikasjoner/rekordhoy-tommerhogst (accessed: 01.03.2020).

Stenlid, J. & Wästerlund, I. (1986). Estimating the Frequency of Stem Rot in Picea abies Using an Increment Borer. *Scandinavian Journal of Forest Research*, 1 (1): 303-308. doi: 10.1080/02827588609382421.

Sundblad, L.-G., Thor, M., Wilhelmsson, L., Linander, F. & Hannertz, M. (2008). *Hjälpmedel för inventering av rotröta i stående skog*. Resultat från Skogforsk 18/2008. Available at: https://www.skogskunskap.se/contentassets/d7f8c00573ef4f71b395aa132a8298d8/skogforsk_resultat_2008_18_hjalpmedel_for_inventering_av_rotrota.pdf (accessed: 24.03.2020).

Suthaharan, S. (2016). *Machine learning models and algorithms for big data classification : thinking with examples for effective learning*. 1st ed. Heidelberg: Springer Science+Business Media. doi: 10.1007/978-1-4899-7641-3.

Terratec AS. (n.d.). *About Terratec AS*. Available at: https://www.terratec.no/en/about-us/ (accessed: 16.04.20).

Thenkabail, P. S., Mariotto, I., Gumma, M. K., Middleton, E. M., Landis, D. R. & Huemmrich, K. F. (2013). Selection of Hyperspectral Narrowbands (HNBs) and Composition of Hyperspectral Twoband Vegetation Indices (HVIs) for Biophysical Characterization and Discrimination of Crop Types Using Field Reflectance and Hyperion/EO-1 Data. *IEEE Journal of Selected Topics in Applied Earth Observations and Remote Sensing*, 6 (2): 427-439. doi: 10.1109/JSTARS.2013.2252601.

Thor, M. (2005). *Heterobasidion root rot in Norway spruce*. Master's thesis. Uppsala: Sveriges lantbruksuniversitet. Available at: https://pub.epsilon.slu.se/729/.

Thor, M., Ståhl, G. & Stenlid, J. (2005). Modelling root rot incidence in Sweden using tree, site and stand variables. *Scandinavian Journal of Forest Research*, 20 (2): 165-176. doi: 10.1080/02827580510008347.

Topcon. (n.d.). *HiPer SR*. Available at: https://www.topconpositioning.com/gnss/integrated-gnss-receivers/hiper-sr (accessed: 16.04.20).

Tveite, B. (1977). *Site index curves for Norway spruce (Picea abies (L.) Karst.)* Reports from the Norwegian Institute for Forest Research 03/1977.

University of Connecticut. (n.d.). *LiDAR*. Illustration. Available at: https://stormwise.uconn.edu/lidar/ (accessed: 14.05.2020).

Vauhkonen, J., Ene, L., Gupta, S., Heinzel, J., Holmgren, J., Pitkänen, J., Solberg, S., Wang, Y., Weinacker, H., Hauglin, K. M., et al. (2011). Comparative testing of single-tree detection algorithms under different types of forest. *Forestry: An International Journal of Forest Research*, 85 (1): 27-40. doi: 10.1093/forestry/cpr051.

Venables, W. N. & Ripley, B. D. (2002). *Modern Applied Statistics with S* (Version 7.3.51.6). R package. Available at: https://cran.r-project.org/web/packages/MASS/index.html (accessed: 15.04.20).

Wang, M., Wright, J., Buswell, R. & Brownlee, A. (2013). A comparison of approches to stepwise regression for global sensitivity analysis used with evolutionary optimization. *13th Conference of International Building Performance Simulation Association*.